

AzTEC/ASTE 1.1-mm survey of SSA22: Counterpart identification and photometric redshift survey of submillimetre galaxies

H. Umehata,^{1*} Y. Tamura,¹ K. Kohno,^{1,2} B. Hatsukade,³ K. S. Scott,⁴ M. Kubo,⁵ T. Yamada,⁵ R. J. Ivison,^{6,7} R. Cybulski,⁸ I. Aretxaga,⁹ J. Austermann,¹⁰ D. H. Hughes,⁹ H. Ezawa,³ T. Hayashino,⁵ S. Ikarashi,¹ D. Iono,^{3,11} R. Kawabe,^{3,12} Y. Matsuda,³ H. Matsuo,¹³ K. Nakanishi,^{3,12,14} T. Oshima,¹¹ T. Perera,⁸ T. Takata,³ G. W. Wilson⁸ and M. S. Yun⁸

¹*Institute of Astronomy, The University of Tokyo, Mitaka, Tokyo 181-0015, Japan*

²*Research Center for the Early Universe (WPI), University of Tokyo, 7-3-1 Hongo, Bunkyo, Tokyo 113-0033, Japan*

³*National Astronomical Observatory of Japan, Mitaka, Tokyo 181-8588, Japan*

⁴*North American ALMA Science Center, National Radio Astronomy Observatory, 520 Edgemont Road, Charlottesville, Virginia 22903, USA*

⁵*Astronomical Institute, Tohoku University, 6-3 Aoba, Aramaki, Aoba-ku, Sendai, Miyagi 980-8578, Japan*

⁶*UK Astronomy Technology Centre, Science and Technology Facilities Council, Royal Observatory, Blackford Hill, Edinburgh EH9 3HJ*

⁷*Institute for Astronomy, University of Edinburgh, Blackford Hill, Edinburgh EH9 3HJ*

⁸*Department of Astronomy, University of Massachusetts, Amherst, MA 01003, USA*

⁹*Instituto Nacional de Astrofísica, Óptica y Electrónica (INAOE), Aptdo. Postal 51 y 216, 72000 Puebla, Pue., Mexico*

¹⁰*Center for Astrophysics and Space Astronomy, University of Colorado, Boulder, CO 80309, USA*

¹¹*Nobeyama Radio Observatory, National Astronomical Observatory of Japan, Minaminaki, Minamisaku, Nagano 384-1305, Japan*

¹²*Joint ALMA Observatory, Alonso de Cordova 3107, Vitacura, Santiago 763 0355, Chile*

¹³*Advanced Technology Center, National Astronomical Observatory of Japan, Mitaka, Tokyo 181-8588, Japan*

¹⁴*The Graduate University for Advanced Studies (Sokendai), Mitaka, Tokyo 181-8588, Japan*

Accepted 2014 March 5. Received 2014 March 5; in original form 2013 November 16

ABSTRACT

We present the results from a 1.1-mm imaging survey of the SSA22 field, known for having an overdensity of $z = 3.1$ Lyman α emitting galaxies (LAEs), taken with the astronomical thermal emission camera (AzTEC) on the Atacama Submillimeter Telescope Experiment (ASTE). We imaged a 950-arcmin^2 field down to a 1σ sensitivity of $0.7\text{--}1.3$ mJy beam⁻¹ to find 125 submillimetre galaxies (SMGs) with a signal-to-noise ratio ≥ 3.5 . Counterpart identification using radio and near/mid-infrared data was performed and one or more counterpart candidates were found for 59 SMGs. Photometric redshifts based on optical to near-infrared images were evaluated for 45 of these SMGs with *Spitzer*/IRAC data and the median value is found to be $z = 2.4$. By combining these estimations with estimates from the literature, we determined that 10 SMGs might lie within the large-scale structure at $z = 3.1$. The two-point angular cross-correlation function between LAEs and SMGs indicates that the positions of the SMGs are correlated with the $z = 3.1$ protocluster. These results suggest that the SMGs were formed and evolved selectively in the high dense environment of the high-redshift Universe. This picture is consistent with the predictions of the standard model of hierarchical structure formation.

Key words: galaxies: distances and redshifts – galaxies: formation – galaxies: high-redshift – large-scale structure of Universe – submillimetre: galaxies.

1 INTRODUCTION

The first deep extragalactic survey at $850\ \mu\text{m}$ undertaken with the Submillimeter Common-User Bolometer Array (SCUBA; Holland et al. 1999) on the James Clerk Maxwell Telescope (JCMT) unveiled a population of galaxies in the distant-redshift Universe that are

extremely bright at submillimetre wavelengths (Smail, Ivison & Blain 1997; Hughes et al. 1998; Barger et al. 1998). This was followed by several wide surveys at (sub)millimetre wavelengths, which were conducted to discover more and more such galaxies (e.g. Greve et al. 2004; Scott et al. 2008; Coppin et al. 2009; Hatsukade et al. 2011).

These submillimetre bright galaxies (SMGs) have huge rest-frame far-infrared (FIR) luminosities ($L_{\text{FIR}} \sim 10^{12}\text{--}10^{13} L_{\odot}$), which should be caused mainly by highly dust-enshrouded star

* E-mail: umehata@ioa.s.u-tokyo.ac.jp

formation and are often indicative of a star-formation rate (SFR) of $\geq 1000 M_{\odot} \text{ yr}^{-1}$. Their flux at submillimetre wavelengths is almost constant for galaxies with a given FIR luminosity at $z \sim 1-10$, due to the negative k -correction. It is hence of great benefit to discover high-redshift objects (for review, see Blain et al. 2002). In addition to their high activity, spectroscopic observations of the millimetre and submillimetre transitions of molecular carbon monoxide (CO) have unveiled the large dynamical and gas masses of SMGs (Greve et al. 2005). This observational evidence shows that SMGs were the most active, massive star-forming galaxies in the early Universe. Clarification of the SMG nature and formation process is seriously important to understand galaxy formation and evolution.

As with other galaxy populations, one of the most crucial questions regarding SMGs is how their formation and evolution depend on their environment. Current cold dark matter (CDM) cosmological simulations show that SMGs should preferentially exist in regions where the mass densities are high and, correspondingly, the merger rates are also high (Springel et al. 2005). SMGs are also supposed to be progenitors of the massive elliptical galaxies seen in the cores of present-day rich clusters (Eales et al. 1999). While the connection between SMGs and massive dark matter haloes has been statistically indicated by clustering analysis (Blain et al. 2004; Williams et al. 2011; Hickox et al. 2012), the connection in individual cluster/protoclusters is still unclear, although previous articles have reported some cases. Capak et al. (2011) and Daddi et al. (2009) reported the discovery of SMGs in overdense regions at $z = 5.3$ and $z = 4.05$, respectively. These results indicate that the overdense regions might be sites of SMG formation. On the other hand, Chapman et al. (2009) shows that SMGs are formed in less overdense regions at $z = 1.99$. Thus the environmental dependence on SMG formation is still controversial.

The relationship between SMGs and the surrounding environment is also intriguing from the viewpoint of galaxy formation in (proto)clusters. In the local Universe, the morphology–density relation is well known. Observations have revealed a higher fraction of early-type galaxies in denser environments (Dressler 1980). This trend has been confirmed for up to a $z \sim 1$ Universe (e.g. Postman et al. 2005). Although this is one of the most established environmental effects on galaxy evolution, it is difficult to examine the relation directly at higher redshifts. Instead, the colour–density or colour–magnitude relations were examined as proxies. For instance, Kodama et al. (2007) examined the colour–magnitude relation in protoclusters and found that the red sequence of galaxies, which is well-established in clusters at least out to $z \sim 1$, first appeared at $z = 2-3$. This suggests that massive galaxies were assembled in protoclusters in this era.

SSA22 is a unique laboratory field to investigate the formation of star-forming galaxies, including SMGs, in overdense regions. Steidel et al. (1998) first discovered this protocluster as a concentration of Lyman-break galaxies (LBGs) at $z = 3.09$. Furthermore, Steidel et al. (2000) found that the surface density of Lyman α emitters (LAEs) was also much higher than that of other fields. Consequently, a wide field survey using Subaru/Suprime-Cam equipped with a narrow-band filter (NB497) has revealed a structure that was traced by LAEs and spread over 700 arcmin^2 (Hayashino et al. 2004; Yamada et al. 2012). Yamada et al. (2012) evaluated that the degree of overdensity was at most 10 times the expected standard deviations based on counts of LAEs at $z = 3.1$. Hence the SSA22 field can provide us with unique insights regarding galaxy formation in an overdense environment. Several previous works on SMGs discovered by SCUBA and astronom-

ical thermal emission camera (AzTEC)/Atacama Submillimeter Telescope Experiment (ASTE) surveys in this field have been reported. Blain et al. (2004) and Chapman et al. (2005) confirmed that three SCUBA SMGs have $z_{\text{spec}} = 3.1$ and these SMGs indeed lie within the densest region. Tamura et al. (2009) showed that there was an angular correlation between the 15 brightest AzTEC SMGs and $z = 3.1$ LAEs.

However, the lack of redshift information prevents us from investigating this further. Although redshift is one of the essential pieces of information required for this purpose, obtaining it has remained a difficult task. First, the typical beam size of the single-dish telescopes used for wide field SMG surveys is insufficient to determine position accurately. In the case of the AzTEC/ASTE survey, we can achieve only ~ 30 arcsec FWHM. Accurate positions of SMGs could ideally be obtained with a submillimetre interferometer, like the Atacama Large Millimeter/submillimetre Array (ALMA), but such observations are time-intensive over large fields. Secondly, SMGs generally tend to be optically faint due to dust attenuation and hence optical observations are often helpless to determine counterparts and obtain redshift information. To overcome such difficulties in searching counterparts and determining redshift, previous works have shown that multiwavelength identification utilizing radio, Multi-Band Imaging Photometer (MIPS: Rieke et al. 2004) and InfraRed Array Camera (IRAC: Fazio et al. 2004) imaging data is useful (Biggs et al. 2011; Wardlow et al. 2011; Yun et al. 2012). If the identified counterparts in these images have an optical to near-infrared counterpart, we can derive a photometric redshift. This is the approach we will follow. We expand the area concerned by Tamura et al. and add photometric redshift information to investigate the relation between SMGs and their underlying environment more closely.

The organization of this article is as follows. In Section 2 we report the general properties of the AzTEC/ASTE survey and the detected SMGs. The utilization of other wavelength data sets for this field is presented in Section 3. In Section 4 we describe our analysis used for counterpart identification. Estimation of photometric redshifts is performed in Section 5. In Section 6 we discuss the relationship between SMGs and the $z = 3.1$ protocluster. We assume a cosmology with $\Omega_m = 0.3$, $\Omega_{\Lambda} = 0.7$, $H_0 = 70 \text{ km s}^{-1} \text{ Mpc}^{-1}$; all magnitudes are given according to the AB system throughout the article.

2 AZTEC/ASTE OBSERVATION

2.1 Observations

We used the AzTEC camera operating at 1.1 mm (Wilson et al. 2008) mounted on the ASTE 10-m submillimetre telescope (Ezawa et al. 2004; Ezawa et al. 2008) located at Pampa la Bola, near Cerro Chajnantor in northern Chile. The AzTEC camera is a 144-element bolometer array and AzTEC/ASTE provides an angular resolution of 28 arcsec in full width at half-maximum (FWHM). All of the AzTEC/ASTE observations of SSA22 were carried out at night during 2007 August–September and 2008 August–September. Some of these data were reported in Tamura et al. (2009) and Tamura et al. (2013). The dry weather at the high site (4860 m in elevation) provided an excellent data set that was taken under $\tau_{220 \text{ GHz}} = 0.01-0.10$. We mapped a 50-arcmin diameter region centred at RA (J2000) = $22^{\text{h}}17^{\text{m}}6$, Dec. (J2000) = $+0^{\circ}15'0$. Observations were made using the on-the-fly (OTF) mode by continuously scanning the telescope bore-sight in azimuth and elevation in a

modified Lissajous scan pattern, which is described as a function of time t by

$$\delta Az = A \sin at + B \sin(at/f), \quad (1)$$

$$\delta El = C \sin bt + D \sin(bt/f). \quad (2)$$

In 2007, we used a scan pattern with $(A, B, C, D, a, b, f) = (7'40'', 7'40'', 3'40'', 3'40'', 5.0, 4.0, 45.0)$. The actual values of a and b are normalized to limit the peak telescope slew velocity to $330 \text{ arcsec s}^{-1}$. In order to go deeper and wider, we used another scan pattern for the 2008 observations with $(A, B, C, D, a, b, f) = (22', 22', 2', 2', 6.0, 5.0, 23)$. The coverage was centred at the same position as those in 2007, but swept a doughnut-like region surrounding the 2007 coverage. The total integrated time on source through 2007–2008 was 74 h. The area of the co-added map where the noise levels are below 1 mJy was estimated to reach 900 arcmin^2 . The wind speeds during the runs were $1\text{--}10 \text{ m s}^{-1}$ and typically 5 m s^{-1} , providing a random telescope pointing offset of $<1 \text{ arcsec}$. The astrometry was checked using a bright quasar 3C446, 5.6 deg away from SSA22, every $1\text{--}1.5 \text{ h}$ during the observations. The correction to the telescope pointing model was small (typically $<2 \text{ arcsec}$) and applied to all scans towards SSA22, resulting in an absolute pointing accuracy better than 4 arcsec (Tamura et al. 2013). For flux calibration, beam-shape measurements and array flat-fielding, beam maps of Uranus and Neptune were taken at least once, typically twice, a night. The beam maps were made so that each bolometer pixel raster-scans and images the planets. The flux calibration accuracy was estimated to be 10 per cent or better.

2.2 Data reduction

The data were reduced in the standard manner described in Scott et al. (2008) and Downes et al. (2012) and we mention only the outline here. We employed an atmospheric noise-removal technique based on principal component analysis (PCA cleaning) to isolate the low-frequency atmospheric noise from the astronomical signals involved in time-stream data. The cleaned time-stream data of each scan were projected on to a map by binning them into $3 \times 3 \text{ arcsec}^2$ pixels and the individual scans were co-added into a single map by weighted averaging.

We also generated 100 noise realizations by jack-knifing the time-stream data (i.e. by multiplying each 15-s time-stream interval by ± 1 randomly and then reducing in the standard manner), which were free of astronomical emission and hence represented the underlying photon noises from the atmosphere and instruments. These random maps were used to estimate a ‘noise map’ by computing pixel-to-pixel standard deviations, which represent the local noise level. We also create a weight map by computing an inverse-square of the noise map. Since the PCA cleaning was AC-coupled to the time stream and hence worked as a high-pass filter (i.e. the resulting map is zero-mean), it attenuated the peak flux and caused negative side lobes around a source. To correct these effects, we simulated the profile of the point-source response function (a point-source kernel) following the method presented in Downes et al. (2012).

2.3 Map and source catalogue

The resulting 1.1-mm map is shown in Fig. 1. In this article, we consider the area where the weight (i.e. inverse square of the noise level) is equal to or greater than 30 per cent of the maximum weight as the survey area. The surface area that AzTEC covered was 0.27 deg^2 , in which the 1σ noise level ranges from $0.7\text{--}1.3 \text{ mJy beam}^{-1}$

(50 per cent of the region has $<0.8 \text{ mJy beam}^{-1}$). The map area corresponds to approximately $60 \times 60 \text{ Mpc}^2$ in a comoving area at $z = 3.1$, which is large enough to cover the protocluster.

The 1.1-mm sources are extracted from the signal-to-noise ratio map, made from the signal map divided by the noise map, with a detection threshold of $\geq 3.5\sigma$. Each source position is defined by flux-squared weighting of the pixels of the nominal peak within a radius of 15 arcsec . We detected 125 sources in the 30 per cent coverage area (Table 1), which are listed in Table 2. $17 \geq 3.5\sigma$ sources were detected in the 10–30 per cent coverage area. These are summarized in a supplementary source catalogue (Table 3).

For a source population with number counts that decrease rapidly with increasing flux density, the measured flux of a low signal-to-noise-ratio (S/N) source can be boosted by random noise. The flux densities of the detected sources are deboosted to correct for this flux bias using the Bayesian recipe described in Coppin et al. (2006) and Scott et al. (2008). To compute the posterior probability distribution function (PDF) of the intrinsic flux densities, we simulated a prior distribution function and a likelihood function at each position where the actual source is detected. In order to estimate the prior distribution function, we made 10^4 maps of photon-noise-free random sky realizations that we would observe with the AzTEC/ASTE kernel according to the best estimate of the 1.1-mm source counts (Scott et al. 2012). By creating a flux histogram across the maps, we arrived at the prior distribution function. We approximated the likelihood function with a normal distribution, with σ being the local noise level at each source position. The PDF was obtained by multiplying the prior and likelihood functions. The deboosted flux is then given by the flux that gives a local maximum of the PDF closest to the measured flux. The deboosted flux and error bars (68 per cent confidence intervals) are also listed in Table 2.

2.4 Characterization of a map

2.4.1 False detections

Some fraction of AzTEC sources were expected to be spurious sources due to positive noise fluctuation, especially when the source had a modest value of S/N. To estimate the number of such non-real sources in the SSA22 map, we extracted sources from a set of jack-knifed noise maps. The standard source extraction procedures were performed for 100 simulated maps within the 30 per cent coverage region. Fig. 2 represents the obtained cumulative false detection rate. The computed number of false detections is shown as a function of S/N. At $S/N \approx 3.5$, approximately 8 out of 125 sources (6 per cent) were predicted to be spurious.

2.4.2 Completeness

The survey completeness is defined as the probability that a real source will result in a measurement above the detection threshold. To evaluate it, we measured the recovery rate of point sources with known flux densities that were embedded into the signal map. The sources were embedded one at a time, using flux densities ranging from $0.5\text{--}8.0 \text{ mJy}$. The input positions were selected randomly within the 30 per cent coverage region. To avoid source blending, the area around a real source (within 20 arcsec) was not permitted for embedding sources. If an input source was detected within 20 arcsec of its embedded position with $S/N \gg 3.5$, it was approved to be recovered. We performed 1000 trials and found that the survey completeness was 50 per cent at a flux density of 2.75 mJy . Fig. 3

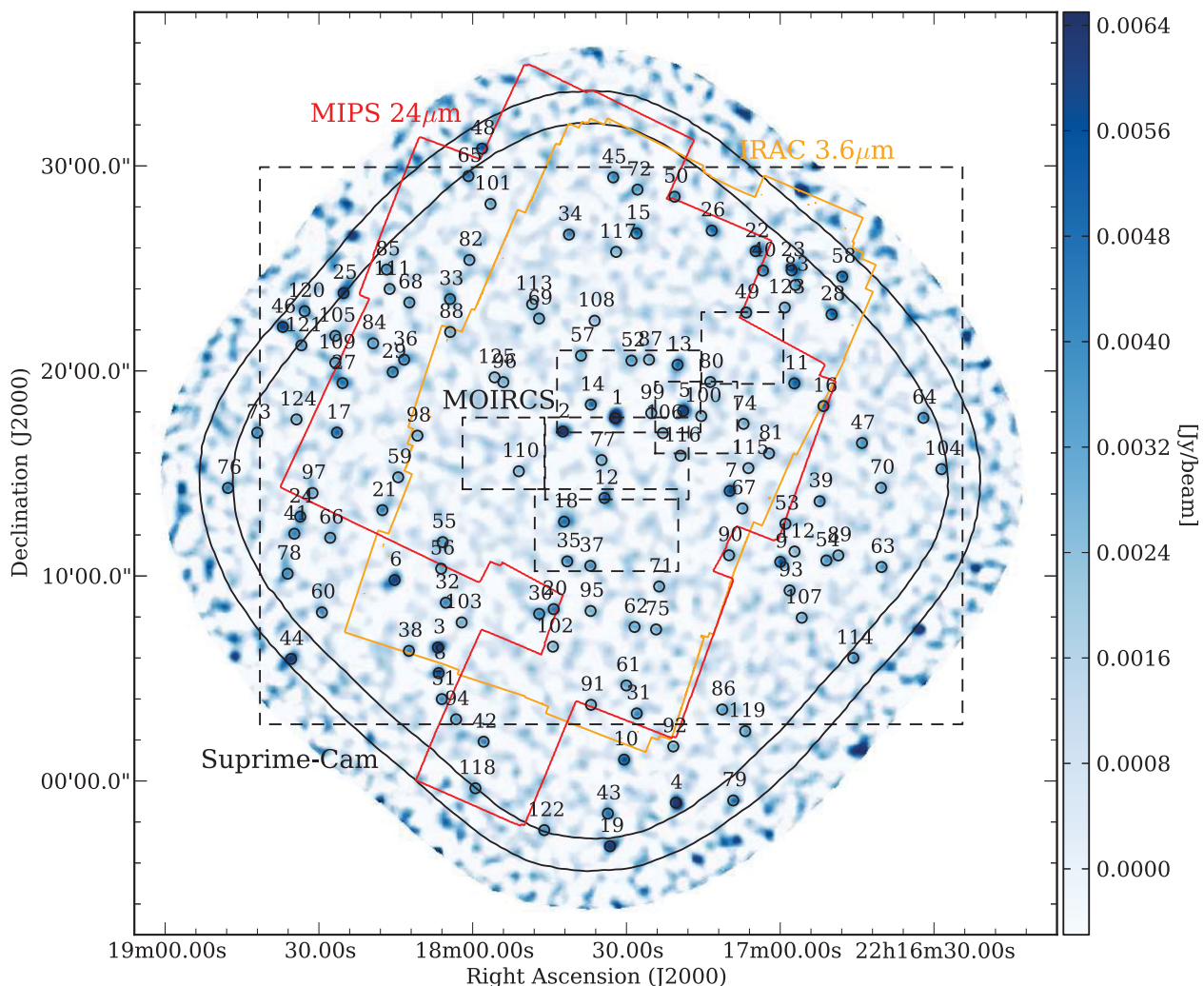


Figure 1. AzTEC/ASTE 1.1 mm image and observation areas of each instrument. The background image is the AzTEC 1.1 mm signal map of the SSA22 field with a 10 per cent uniform coverage region. The sidebar represents flux density in units of Jy beam^{-1} . The 30 and 50 per cent coverage regions are shown using black contours. The black circles indicate the positions of $\geq 3.5\sigma$ sources and the diameter is 30 arcsec, which corresponds to the FWHM of AzTEC/ASTE. In addition, the areas of Suprime-Cam (large dashed rectangle), MIPS 24- μm (red line), IRAC 3.6- μm (yellow line) and MOIRCS (small dashed rectangle) are shown. The UKIRT/DXS survey and VLA 1.4-GHz observations contain all AzTEC sources.

Table 1. Map properties in the 50 per cent and 30–50 per cent coverage regions. $N(\text{source})$ and $N(\text{False})$ show number of sources and false detections ($\leq 3.5\sigma$ for both).

Coverage	Area [arcmin^2]	Noise level [mJy beam^{-1}]	$N(\text{Source})$	$N(\text{False})$
50%	749	0.72–1.00	107	6.2 ± 2.4
30–50%	205	1.00–1.32	18	2.4 ± 0.8

shows the differential completeness as a function of flux density. The error bars were calculated assuming a binomial distribution.

2.4.3 Positional uncertainty

The detected position of a 1.1-mm source is affected by random and confusion noise in the map, which leads to a large positional error. We estimated such positional uncertainty in a way similar to the one in Section 2.4.2. A point source was inserted with known flux density into the SSA22 signal map. We extracted it using a

standard algorithm and measured the distribution of input to output source distances as a function of S/N. We repeated these processes for three sample S/N bins ($3.5 \leq S/N < 4.5$, $4.5 \leq S/N < 5.5$ and $5.5 \leq S/N < 9.0$). Fig. 4 shows the probability that a source detected with a given S/N will be found outside a radial distance θ from its intrinsic position.

3 MULTIWAVELENGTH DATA AND CATALOGUEING

We utilized optical-to-radio multiwavelength imaging data to search for counterparts of SMGs discovered by the AzTEC/ASTE survey and estimated the photometric redshift, though most of these observations did not cover the survey area completely, as shown in Fig. 1. For counterpart identification we employed Very Large Array (VLA) 1.4-GHz, MIPS 24- μm and IRAC 3.6–8.0 μm data, all described in more detail below. Then, in addition to the IRAC data, optical to near-infrared photometry data taken with the Canada–France–Hawaii Telescope (CFHT)/Mega-Cam,

Table 2. The AzTEC/ASTE SSA22 source catalogue. The machine-readable version is available online. Columns are as follows: (1) source name; (2) AzTEC source ID; (3) Right Ascension; (4) Declination; (5) observed 1.1-mm flux density and 1σ error; (6) deboosted 1.1-mm flux density and 68 per cent confidence interval; (7) signal-to-noise ratio of the detection in the AzTEC map.

Name	ID	RA [$^{\text{h}} \text{ }^{\text{m}} \text{ }^{\text{s}}$]	Dec. [$^{\circ} \text{ }^{\prime}$ arcsec]	S_{observed} [mJy]	$S_{\text{deboosted}}$ [mJy]	S/N
AzTEC J221732.21+001742.1	SSA22-AzTEC1	22 17 32.21	+00 17 42.1	11.9 ± 0.7	$11.3^{+0.9}_{-0.7}$	16.2
AzTEC J221742.42+001702.5	SSA22-AzTEC2	22 17 42.42	+00 17 02.5	7.5 ± 0.7	$6.9^{+0.9}_{-0.7}$	10.1
AzTEC J221806.78+000630.6	SSA22-AzTEC3	22 18 06.78	+00 06 30.6	7.4 ± 0.8	$6.9^{+0.8}_{-0.9}$	9.4
AzTEC J221720.36-000103.6	SSA22-AzTEC4	22 17 20.36	-00 01 03.6	9.4 ± 1.0	$8.5^{+1.1}_{-1.1}$	9.2
AzTEC J221718.95+001803.0	SSA22-AzTEC5	22 17 18.95	+00 18 03.0	6.6 ± 0.7	$6.1^{+0.8}_{-0.8}$	8.9
AzTEC J221815.23+000948.0	SSA22-AzTEC6	22 18 15.23	+00 09 48.0	6.5 ± 0.8	$5.9^{+0.8}_{-0.8}$	8.5
AzTEC J221709.85+001408.9	SSA22-AzTEC7	22 17 09.85	+00 14 08.9	6.1 ± 0.7	$5.6^{+0.8}_{-0.8}$	8.3
AzTEC J221806.62+000515.7	SSA22-AzTEC8	22 18 06.62	+00 05 15.7	6.2 ± 0.8	$5.7^{+0.8}_{-0.9}$	7.7
AzTEC J221700.00+001041.2	SSA22-AzTEC9	22 17 00.00	+00 10 41.2	5.8 ± 0.8	$5.3^{+0.8}_{-0.8}$	7.7
AzTEC J221730.46+000102.5	SSA22-AzTEC10	22 17 30.46	+00 01 02.5	5.9 ± 0.8	$5.3^{+0.9}_{-0.9}$	7.3
AzTEC J221657.24+001923.6	SSA22-AzTEC11	22 16 57.24	+00 19 23.6	5.5 ± 0.8	$4.9^{+0.9}_{-0.8}$	7.2
AzTEC J221734.30+001348.2	SSA22-AzTEC12	22 17 34.30	+00 13 48.2	5.4 ± 0.8	$4.9^{+0.8}_{-0.8}$	7.1
AzTEC J221720.03+002017.9	SSA22-AzTEC13	22 17 20.03	+00 20 17.9	5.2 ± 0.7	$4.6^{+0.8}_{-0.8}$	7.0
AzTEC J221736.96+001821.3	SSA22-AzTEC14	22 17 36.96	+00 18 21.3	5.0 ± 0.7	$4.5^{+0.8}_{-0.8}$	6.9
AzTEC J221728.04+002642.6	SSA22-AzTEC15	22 17 28.04	+00 26 42.6	5.3 ± 0.8	$4.7^{+0.9}_{-0.8}$	6.8
AzTEC J221651.56+001817.2	SSA22-AzTEC16	22 16 51.56	+00 18 17.2	5.2 ± 0.8	$4.6^{+0.9}_{-0.8}$	6.7
AzTEC J221826.48+001659.6	SSA22-AzTEC17	22 18 26.48	+00 16 59.6	5.1 ± 0.8	$4.5^{+0.8}_{-0.8}$	6.5
AzTEC J221742.18+001238.8	SSA22-AzTEC18	22 17 42.18	+00 12 38.8	4.8 ± 0.7	$4.3^{+0.8}_{-0.8}$	6.5
AzTEC J221733.21-000310.8	SSA22-AzTEC19	22 17 33.21	-00 03 10.8	7.5 ± 1.2	$6.3^{+1.2}_{-1.2}$	6.5
AzTEC J221744.20+000822.9	SSA22-AzTEC20	22 17 44.20	+00 08 22.9	4.5 ± 0.7	$4.0^{+0.8}_{-0.8}$	6.2
AzTEC J221817.62+001312.6	SSA22-AzTEC21	22 18 17.62	+00 13 12.6	4.6 ± 0.7	$4.0^{+0.8}_{-0.8}$	6.1
AzTEC J221704.79+002550.6	SSA22-AzTEC22	22 17 04.79	+00 25 50.6	5.7 ± 0.9	$4.8^{+1.0}_{-1.0}$	6.1
AzTEC J221657.77+002454.3	SSA22-AzTEC23	22 16 57.77	+00 24 54.3	5.9 ± 1.0	$5.0^{+1.0}_{-1.1}$	6.1
AzTEC J221833.64+001253.6	SSA22-AzTEC24	22 18 33.64	+00 12 53.6	5.0 ± 0.8	$4.4^{+0.9}_{-0.9}$	6.1
AzTEC J221825.20+002347.9	SSA22-AzTEC25	22 18 25.20	+00 23 47.9	6.6 ± 1.1	$5.5^{+1.2}_{-1.2}$	6.0
AzTEC J221713.37+002650.8	SSA22-AzTEC26	22 17 13.37	+00 26 50.8	5.1 ± 0.9	$4.4^{+0.9}_{-1.0}$	5.9
AzTEC J221825.40+001924.5	SSA22-AzTEC27	22 18 25.40	+00 19 24.5	4.9 ± 0.8	$4.2^{+0.9}_{-0.9}$	5.9
AzTEC J221649.97+002245.2	SSA22-AzTEC28	22 16 49.97	+00 22 45.2	5.5 ± 0.9	$4.7^{+1.0}_{-1.1}$	5.8
AzTEC J221815.60+001956.7	SSA22-AzTEC29	22 18 15.60	+00 19 56.7	4.5 ± 0.8	$3.8^{+0.9}_{-0.8}$	5.8
AzTEC J221747.03+000809.0	SSA22-AzTEC30	22 17 47.03	+00 08 09.0	4.2 ± 0.7	$3.7^{+0.8}_{-0.8}$	5.8
AzTEC J221727.99+000317.6	SSA22-AzTEC31	22 17 27.99	+00 03 17.6	4.3 ± 0.8	$3.7^{+0.8}_{-0.8}$	5.7
AzTEC J221805.25+000841.8	SSA22-AzTEC32	22 18 05.25	+00 08 41.8	4.2 ± 0.8	$3.7^{+0.8}_{-0.9}$	5.6
AzTEC J221804.42+002330.4	SSA22-AzTEC33	22 18 04.42	+00 23 30.4	4.4 ± 0.8	$3.8^{+0.9}_{-0.9}$	5.6
AzTEC J221741.21+002639.0	SSA22-AzTEC34	22 17 41.21	+00 26 39.0	4.3 ± 0.8	$3.7^{+0.8}_{-0.8}$	5.6
AzTEC J221741.56+001042.7	SSA22-AzTEC35	22 17 41.56	+00 10 42.7	4.1 ± 0.7	$3.5^{+0.8}_{-0.8}$	5.5
AzTEC J221813.38+002032.9	SSA22-AzTEC36	22 18 13.38	+00 20 32.9	4.2 ± 0.8	$3.6^{+0.8}_{-0.9}$	5.4
AzTEC J221737.05+001029.7	SSA22-AzTEC37	22 17 37.05	+00 10 29.7	4.0 ± 0.7	$3.4^{+0.8}_{-0.8}$	5.4
AzTEC J221812.44+000620.8	SSA22-AzTEC38	22 18 12.44	+00 06 20.8	4.3 ± 0.8	$3.6^{+0.9}_{-0.9}$	5.3
AzTEC J221652.32+001338.6	SSA22-AzTEC39	22 16 52.32	+00 13 38.6	3.9 ± 0.8	$3.3^{+0.8}_{-0.8}$	5.2
AzTEC J221703.36+002453.6	SSA22-AzTEC40	22 17 03.36	+00 24 53.6	4.6 ± 0.9	$3.8^{+1.0}_{-1.0}$	5.2
AzTEC J221834.80+001203.5	SSA22-AzTEC41	22 18 34.80	+00 12 03.5	4.5 ± 0.9	$3.7^{+0.9}_{-1.0}$	5.2
AzTEC J221757.87+000154.9	SSA22-AzTEC42	22 17 57.87	+00 01 54.9	4.5 ± 0.9	$3.7^{+0.9}_{-1.0}$	5.1
AzTEC J221733.63-000135.4	SSA22-AzTEC43	22 17 33.63	-00 01 35.4	4.8 ± 1.0	$3.9^{+1.0}_{-1.0}$	5.1
AzTEC J221835.43+000557.3	SSA22-AzTEC44	22 18 35.43	+00 05 57.3	6.8 ± 1.3	$5.0^{+1.5}_{-1.4}$	5.0
AzTEC J221732.59+002926.4	SSA22-AzTEC45	22 17 32.59	+00 29 26.4	4.3 ± 0.9	$3.5^{+1.0}_{-0.9}$	5.0
AzTEC J221837.04+002208.7	SSA22-AzTEC46	22 18 37.04	+00 22 08.7	6.5 ± 1.3	$4.8^{+1.5}_{-1.4}$	5.0
AzTEC J221644.05+001629.1	SSA22-AzTEC47	22 16 44.05	+00 16 29.1	3.9 ± 0.8	$3.2^{+0.9}_{-0.9}$	4.8
AzTEC J221758.17+003050.5	SSA22-AzTEC48	22 17 58.17	+00 30 50.5	5.7 ± 1.2	$4.3^{+1.3}_{-1.3}$	4.8

Table 2 – continued

Name	ID	RA [^h ^m ^s]	Dec. [^o ' arcsec]	S_{observed} [mJy]	$S_{\text{deboosted}}$ [mJy]	S/N
AzTEC J221706.64+002250.9	SSA22-AzTEC49	22 17 06.64	+00 22 50.9	3.8 ± 0.8	3.1 ^{+0.9} _{-0.9}	4.8
AzTEC J221720.60+002829.8	SSA22-AzTEC50	22 17 20.60	+00 28 29.8	4.3 ± 0.9	3.4 ^{+1.0} _{-1.0}	4.8
AzTEC J221806.03+000359.6	SSA22-AzTEC51	22 18 06.03	+00 03 59.6	4.1 ± 0.9	3.3 ^{+0.9} _{-1.0}	4.7
AzTEC J221729.02+002030.2	SSA22-AzTEC52	22 17 29.02	+00 20 30.2	3.5 ± 0.7	2.9 ^{+0.8} _{-0.8}	4.7
AzTEC J221658.98+001232.7	SSA22-AzTEC53	22 16 58.98	+00 12 32.7	3.5 ± 0.7	2.8 ^{+0.9} _{-0.8}	4.7
AzTEC J221650.99+001045.2	SSA22-AzTEC54	22 16 50.99	+00 10 45.2	3.7 ± 0.8	3.0 ^{+0.9} _{-0.9}	4.6
AzTEC J221805.86+001139.0	SSA22-AzTEC55	22 18 05.86	+00 11 39.0	3.3 ± 0.7	2.7 ^{+0.8} _{-0.8}	4.6
AzTEC J221806.15+001021.2	SSA22-AzTEC56	22 18 06.15	+00 10 21.2	3.3 ± 0.7	2.7 ^{+0.8} _{-0.8}	4.5
AzTEC J221738.86+002044.8	SSA22-AzTEC57	22 17 38.86	+00 20 44.8	3.3 ± 0.7	2.7 ^{+0.8} _{-0.8}	4.5
AzTEC J221647.90+002435.6	SSA22-AzTEC58	22 16 47.90	+00 24 35.6	5.2 ± 1.2	3.8 ^{+1.3} _{-1.4}	4.4
AzTEC J221814.53+001448.8	SSA22-AzTEC59	22 18 14.53	+00 14 48.8	3.2 ± 0.7	2.6 ^{+0.8} _{-0.8}	4.4
AzTEC J221829.42+000813.4	SSA22-AzTEC60	22 18 29.42	+00 08 13.4	4.1 ± 0.9	3.1 ^{+1.1} _{-1.0}	4.4
AzTEC J221730.02+000439.6	SSA22-AzTEC61	22 17 30.02	+00 04 39.6	3.3 ± 0.7	2.6 ^{+0.8} _{-0.8}	4.4
AzTEC J221728.42+000730.7	SSA22-AzTEC62	22 17 28.42	+00 07 30.7	3.2 ± 0.7	2.6 ^{+0.8} _{-0.9}	4.4
AzTEC J221640.23+001026.1	SSA22-AzTEC63	22 16 40.23	+00 10 26.1	4.0 ± 0.9	3.0 ^{+1.1} _{-1.0}	4.4
AzTEC J221632.06+001742.5	SSA22-AzTEC64	22 16 32.06	+00 17 42.5	4.4 ± 1.0	3.3 ^{+1.2} _{-1.2}	4.3
AzTEC J221800.83+002930.1	SSA22-AzTEC65	22 18 00.83	+00 29 30.1	4.6 ± 1.1	3.4 ^{+1.2} _{-1.2}	4.3
AzTEC J221827.80+001151.7	SSA22-AzTEC66	22 18 27.80	+00 11 51.7	3.4 ± 0.8	2.7 ^{+0.9} _{-0.9}	4.3
AzTEC J221707.38+001317.5	SSA22-AzTEC67	22 17 07.38	+00 13 17.5	3.1 ± 0.7	2.5 ^{+0.8} _{-0.8}	4.3
AzTEC J221812.36+002320.2	SSA22-AzTEC68	22 18 12.36	+00 23 20.2	3.6 ± 0.8	2.8 ^{+0.9} _{-1.0}	4.3
AzTEC J221747.05+002233.2	SSA22-AzTEC69	22 17 47.05	+00 22 33.2	3.1 ± 0.7	2.5 ^{+0.8} _{-0.8}	4.3
AzTEC J221640.34+001417.9	SSA22-AzTEC70	22 16 40.34	+00 14 17.9	3.5 ± 0.8	2.7 ^{+0.9} _{-0.9}	4.3
AzTEC J221723.62+000929.1	SSA22-AzTEC71	22 17 23.62	+00 09 29.1	3.1 ± 0.7	2.5 ^{+0.8} _{-0.8}	4.2
AzTEC J221727.84+002850.6	SSA22-AzTEC72	22 17 27.84	+00 28 50.6	3.6 ± 0.9	2.8 ^{+0.9} _{-1.0}	4.2
AzTEC J221842.03+001659.3	SSA22-AzTEC73	22 18 42.03	+00 16 59.3	4.2 ± 1.0	3.1 ^{+1.1} _{-1.1}	4.2
AzTEC J221707.16+001725.2	SSA22-AzTEC74	22 17 07.16	+00 17 25.2	3.1 ± 0.7	2.4 ^{+0.9} _{-0.8}	4.2
AzTEC J221724.22+000723.5	SSA22-AzTEC75	22 17 24.22	+00 07 23.5	3.1 ± 0.7	2.4 ^{+0.8} _{-0.8}	4.2
AzTEC J221847.75+001417.5	SSA22-AzTEC76	22 18 47.75	+00 14 17.5	4.7 ± 1.1	3.3 ^{+1.3} _{-1.4}	4.1
AzTEC J221734.86+001539.2	SSA22-AzTEC77	22 17 34.86	+00 15 39.2	3.2 ± 0.8	2.4 ^{+0.9} _{-0.8}	4.1
AzTEC J221836.10+001006.5	SSA22-AzTEC78	22 18 36.10	+00 10 06.5	3.9 ± 1.0	2.9 ^{+1.1} _{-1.1}	4.1
AzTEC J221709.16−000057.0	SSA22-AzTEC79	22 17 09.16	−00 00 57.0	5.1 ± 1.3	3.4 ^{+1.5} _{-1.5}	4.1
AzTEC J221713.64+001927.5	SSA22-AzTEC80	22 17 13.64	+00 19 27.5	3.0 ± 0.7	2.3 ^{+0.9} _{-0.8}	4.1
AzTEC J221702.19+001558.6	SSA22-AzTEC81	22 17 02.19	+00 15 58.6	3.0 ± 0.7	2.3 ^{+0.9} _{-0.8}	4.1
AzTEC J221800.65+002524.7	SSA22-AzTEC82	22 18 00.65	+00 25 24.7	3.3 ± 0.8	2.5 ^{+0.9} _{-0.9}	4.1
AzTEC J221657.04+002411.5	SSA22-AzTEC83	22 16 57.04	+00 24 11.5	3.8 ± 0.9	2.7 ^{+1.1} _{-1.0}	4.0
AzTEC J221819.43+002120.9	SSA22-AzTEC84	22 18 19.43	+00 21 20.9	3.3 ± 0.8	2.5 ^{+1.0} _{-0.9}	4.0
AzTEC J221816.78+002456.6	SSA22-AzTEC85	22 18 16.78	+00 24 56.6	3.9 ± 1.0	2.8 ^{+1.2} _{-1.1}	4.0
AzTEC J221711.31+000329.2	SSA22-AzTEC86	22 17 11.31	+00 03 29.2	3.3 ± 0.8	2.5 ^{+1.0} _{-1.0}	4.0
AzTEC J221725.60+002032.9	SSA22-AzTEC87	22 17 25.60	+00 20 32.9	2.9 ± 0.7	2.3 ^{+0.8} _{-0.9}	4.0
AzTEC J221804.39+002154.0	SSA22-AzTEC88	22 18 04.39	+00 21 54.0	3.0 ± 0.8	2.3 ^{+0.9} _{-0.9}	4.0
AzTEC J221648.67+001100.2	SSA22-AzTEC89	22 16 48.67	+00 11 00.2	3.2 ± 0.8	2.4 ^{+0.9} _{-0.9}	3.9
AzTEC J221709.98+001100.5	SSA22-AzTEC90	22 17 09.98	+00 11 00.5	2.9 ± 0.7	2.2 ^{+0.9} _{-0.8}	3.9
AzTEC J221736.92+000342.9	SSA22-AzTEC91	22 17 36.92	+00 03 42.9	2.9 ± 0.8	2.2 ^{+0.9} _{-0.8}	3.9
AzTEC J221720.86+000141.0	SSA22-AzTEC92	22 17 20.86	+00 01 41.0	3.2 ± 0.8	2.4 ^{+1.0} _{-1.0}	3.9
AzTEC J221658.17+000917.7	SSA22-AzTEC93	22 16 58.17	+00 09 17.7	3.0 ± 0.8	2.3 ^{+0.9} _{-0.9}	3.9
AzTEC J221803.24+000300.6	SSA22-AzTEC94	22 18 03.24	+00 03 00.6	3.4 ± 0.9	2.5 ^{+1.0} _{-1.0}	3.9
AzTEC J221736.99+000817.5	SSA22-AzTEC95	22 17 36.99	+00 08 17.5	2.8 ± 0.7	2.2 ^{+0.8} _{-0.9}	3.9
AzTEC J221754.02+001927.4	SSA22-AzTEC96	22 17 54.02	+00 19 27.4	2.8 ± 0.7	2.2 ^{+0.8} _{-0.9}	3.9
AzTEC J221831.24+001402.7	SSA22-AzTEC97	22 18 31.24	+00 14 02.7	3.1 ± 0.8	2.3 ^{+0.9} _{-0.9}	3.9
AzTEC J221810.78+001650.5	SSA22-AzTEC98	22 18 10.78	+00 16 50.5	2.9 ± 0.7	2.2 ^{+0.8} _{-0.9}	3.9
AzTEC J221725.16+001756.8	SSA22-AzTEC99	22 17 25.16	+00 17 56.8	2.9 ± 0.7	2.2 ^{+0.8} _{-0.9}	3.9

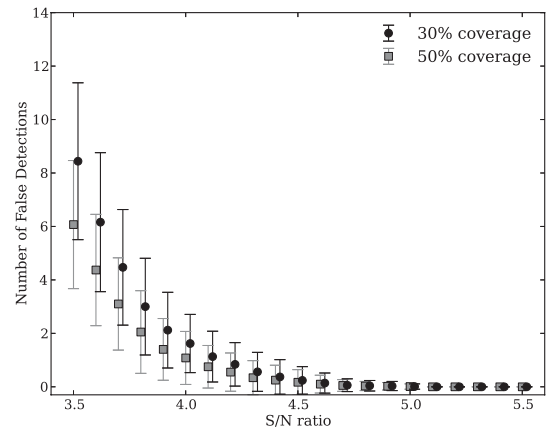
Table 2 – *continued*

Name	ID	RA [^h ^m ^s]	Dec. [[°] ['] ^{arcsec}]	S_{observed} [mJy]	$S_{\text{deboosted}}$ [mJy]	S/N
AzTEC J221715.40+001747.9	SSA22-AzTEC100	22 17 15.40	+00 17 47.9	2.8 ± 0.7	$2.2^{+0.8}_{-0.9}$	3.8
AzTEC J221756.53+002808.6	SSA22-AzTEC101	22 17 56.53	+00 28 08.6	3.4 ± 0.9	$2.5^{+1.0}_{-1.1}$	3.8
AzTEC J221744.34+000633.1	SSA22-AzTEC102	22 17 44.34	+00 06 33.1	2.8 ± 0.7	$2.1^{+0.9}_{-0.8}$	3.8
AzTEC J221802.15+000744.0	SSA22-AzTEC103	22 18 02.15	+00 07 44.0	2.9 ± 0.8	$2.2^{+0.9}_{-0.9}$	3.8
AzTEC J221628.56+001512.6	SSA22-AzTEC104	22 16 28.56	+00 15 12.6	4.0 ± 1.0	$2.7^{+1.3}_{-1.3}$	3.8
AzTEC J221826.81+002142.5	SSA22-AzTEC105	22 18 26.81	+00 21 42.5	3.6 ± 1.0	$2.5^{+1.1}_{-1.1}$	3.8
AzTEC J221722.90+001657.8	SSA22-AzTEC106	22 17 22.90	+00 16 57.8	2.8 ± 0.7	$2.1^{+0.8}_{-0.9}$	3.8
AzTEC J221655.79+000757.7	SSA22-AzTEC107	22 16 55.79	+00 07 57.7	3.1 ± 0.8	$2.3^{+1.0}_{-1.0}$	3.8
AzTEC J221736.21+002226.9	SSA22-AzTEC108	22 17 36.21	+00 22 26.9	2.8 ± 0.7	$2.1^{+0.8}_{-0.9}$	3.8
AzTEC J221826.80+002023.9	SSA22-AzTEC109	22 18 26.80	+00 20 23.9	3.3 ± 0.9	$2.3^{+1.1}_{-1.0}$	3.7
AzTEC J221751.00+001506.4	SSA22-AzTEC110	22 17 51.00	+00 15 06.4	2.7 ± 0.7	$2.1^{+0.8}_{-0.9}$	3.7
AzTEC J221816.21+002359.9	SSA22-AzTEC111	22 18 16.21	+00 23 59.9	3.4 ± 0.9	$2.4^{+1.0}_{-1.1}$	3.7
AzTEC J221657.21+001111.6	SSA22-AzTEC112	22 16 57.21	+00 11 11.6	2.8 ± 0.8	$2.1^{+0.9}_{-0.9}$	3.7
AzTEC J221748.40+002315.2	SSA22-AzTEC113	22 17 48.40	+00 23 15.2	2.7 ± 0.7	$2.0^{+0.9}_{-0.9}$	3.7
AzTEC J221645.74+000600.1	SSA22-AzTEC114	22 16 45.74	+00 06 00.1	4.2 ± 1.1	$0.0^{+1.5}_{-1.4}$	3.7
AzTEC J221706.21+001515.6	SSA22-AzTEC115	22 17 06.21	+00 15 15.6	2.7 ± 0.7	$2.0^{+0.9}_{-0.9}$	3.6
AzTEC J221719.43+001552.0	SSA22-AzTEC116	22 17 19.43	+00 15 52.0	2.7 ± 0.7	$2.0^{+0.8}_{-0.9}$	3.6
AzTEC J221732.01+002548.4	SSA22-AzTEC117	22 17 32.01	+00 25 48.4	2.8 ± 0.8	$2.0^{+0.9}_{-0.9}$	3.6
AzTEC J221759.46-000021.4	SSA22-AzTEC118	22 17 59.46	-00 00 21.4	4.0 ± 1.1	$2.6^{+1.3}_{-1.4}$	3.6
AzTEC J221706.83+000225.8	SSA22-AzTEC119	22 17 06.83	+00 02 25.8	3.4 ± 0.9	$2.3^{+1.2}_{-1.1}$	3.6
AzTEC J221832.78+002254.9	SSA22-AzTEC120	22 18 32.78	+00 22 54.9	4.5 ± 1.2	$0.0^{+1.6}_{-1.6}$	3.6
AzTEC J221833.42+002114.9	SSA22-AzTEC121	22 18 33.42	+00 21 14.9	3.9 ± 1.1	$0.0^{+1.3}_{-1.4}$	3.6
AzTEC J221746.04-000223.9	SSA22-AzTEC122	22 17 46.04	-00 02 23.9	3.9 ± 1.1	$0.0^{+1.3}_{-1.4}$	3.6
AzTEC J221659.11+002305.5	SSA22-AzTEC123	22 16 59.11	+00 23 05.5	3.0 ± 0.8	$2.1^{+1.0}_{-1.1}$	3.5
AzTEC J221834.38+001738.1	SSA22-AzTEC124	22 18 34.38	+00 17 38.1	3.1 ± 0.9	$2.1^{+1.1}_{-1.1}$	3.5
AzTEC J221755.73+001941.3	SSA22-AzTEC125	22 17 55.73	+00 19 41.3	2.6 ± 0.7	$1.9^{+0.9}_{-0.9}$	3.5

Table 3. Supplementary catalogue of AzTEC SMGs detected in the edge (10–30 per cent coverage) region.

ID	R.A. [^h ^m ^s]	Dec. [[°] ['] ^{arcsec}]	S_{observed} [mJy]	S/N
SSA22-AzTEC-Sup1	22 16 56.16	+00 28 43.1	10.3	6.6
SSA22-AzTEC-Sup2	22 16 33.20	+00 07 23.6	8.7	6.0
SSA22-AzTEC-Sup3	22 18 23.56	+00 26 31.1	7.5	5.5
SSA22-AzTEC-Sup4	22 16 22.10	+00 10 21.7	7.3	4.4
SSA22-AzTEC-Sup5	22 18 07.01	-00 03 29.6	9.9	4.3
SSA22-AzTEC-Sup6	22 17 16.35	-00 03 48.0	6.9	4.2
SSA22-AzTEC-Sup7	22 16 34.92	+00 22 30.7	5.4	4.0
SSA22-AzTEC-Sup8	22 16 23.96	+00 21 39.5	7.9	4.0
SSA22-AzTEC-Sup9	22 16 44.60	+00 01 32.5	8.3	4.0
SSA22-AzTEC-Sup10	22 17 08.81	-00 02 53.6	6.6	3.8
SSA22-AzTEC-Sup11	22 18 20.10	+00 02 03.3	5.3	3.8
SSA22-AzTEC-Sup12	22 18 46.36	+00 06 03.7	7.7	3.7
SSA22-AzTEC-Sup13	22 18 52.95	+00 15 19.2	5.2	3.7
SSA22-AzTEC-Sup14	22 18 51.39	+00 10 27.2	5.8	3.7
SSA22-AzTEC-Sup15	22 18 56.75	+00 14 10.2	6.3	3.7
SSA22-AzTEC-Sup16	22 18 24.77	+00 28 05.7	6.3	3.6
SSA22-AzTEC-Sup17	22 16 38.97	+00 05 33.9	5.2	3.5

Subaru/Suprime-Cam, Multi-Object InfraRed Camera and Spectrograph (MOIRCS) and the United Kingdom InfraRed Telescope (UKIRT) were utilized to derive the photometric redshift.

**Figure 2.** Cumulative number count of false detections as a function of the signal-to-noise ratio. The error bars represent 1σ Poisson uncertainties. Circles and squares represent 50 and 30 per cent coverage fields, respectively. Data points for the 30 per cent coverage field are displaced by $+0.02$ in the S/N ratio for clarity.

3.1 VLA 1.4 GHz

The region centred on the coordinate (RA, Dec)_{J2000} = (22^h17^m48.0^s, +00[°]17′13″) was observed for a total of 48 h at 1.4 GHz using the National Radio Astronomy Observatory’s (NRAO’s) Very Large Array (VLA) in its A and B

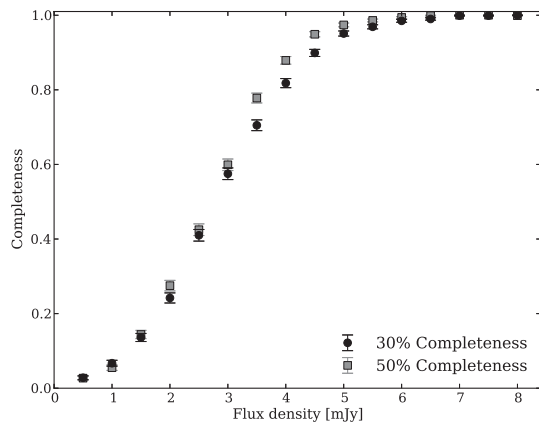


Figure 3. Completeness of the AzTEC/ASTE survey in 50 and 30 per cent coverage fields. The error bars represent 1σ estimated from the binomial distribution.

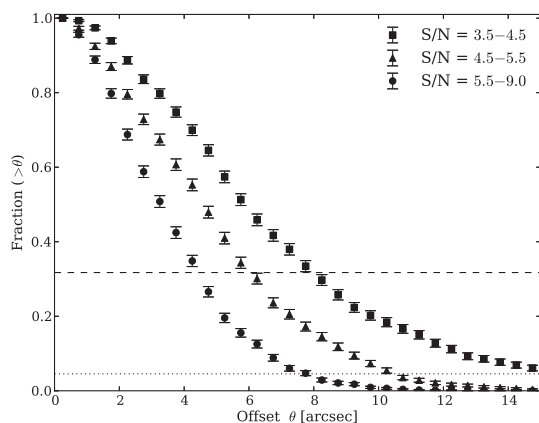


Figure 4. Positional uncertainties estimated from the cumulative probability distribution for a source detected at a position θ arcsec away from the true position. The probability was calculated for sources with $3.5 \leq S/N < 4.5$, $4.5 \leq S/N < 5.5$ and $5.5 \leq S/N < 9.0$. The horizontal dashed and dotted lines represent 68.3 and 99.5 per cent confidence levels, respectively.

configurations (Chapman et al. 2004). Our imaging applied a 50 kλ Gaussian taper to reduce the bandwidth smearing. This produced a well-behaved synthesized beam of 3.0×2.9 arcsec² at a position angle of -80 deg. Generally, a root-mean-square (r.m.s.) noise level of $\sim 8.5 \mu\text{Jy beam}^{-1}$ was achieved near the phase centre and $\sim 20 \mu\text{Jy}$ at 15 arcmin from the phase centre. Unfortunately, the radio map was partly contaminated by remarkable side lobes, which were generated by nearby radio-loud sources. Therefore, to avoid misidentification when cataloguing the radio sources we eliminated areas with a local noise level of $\geq 20 \mu\text{Jy beam}^{-1}$ in cataloguing radio sources. The local noise was estimated using the AIPS task RMSD, in a 100×100 pixel region centred on each pixel. To generate a source catalogue and to measure source properties, we used the task SAD. Finally, 40 radio sources were detected with S/N of ≥ 4 for 66 SMGs.

3.2 *Spitzer*/MIPS, IRAC

In the SSA22 field, several archival *Spitzer* near- to mid-infrared imaging observations are available and IRAC ch1–ch4 (3.6, 4.5, 5.8 and $8.0 \mu\text{m}$) and MIPS ch1 ($24 \mu\text{m}$) images were obtained through the *Spitzer* Science Center (SSC) web site. As shown in

Table 4. Summary of optical to near-/mid-infrared photometry employed in this article.

Band	λ_{eff} (μm)	5σ Depth (mag)	Ref
CFHT/MegaCam			
<i>Un</i>	0.28	26.1	1
Subaru/Suprime-Cam			
<i>B</i>	0.44	26.5	2
NB497	0.50	26.2	2
<i>V</i>	0.54	26.6	2
<i>R</i>	0.65	26.7	2
<i>i'</i>	0.77	26.4	2
<i>z'</i>	0.92	25.7	2
Subaru/MOIRCS			
<i>J</i>	1.25	24.5	3
<i>H</i>	1.64	24.3	3
<i>Ks</i>	2.15	23.9	3
UKIRT/WFCAM			
<i>J</i>	1.26	23.3	4
<i>K</i>	2.24	22.7	4
<i>Spitzer</i> /IRAC			
ch1	3.56	24.9 ^a	5
ch2	4.51	24.1 ^a	5
ch3	5.76	22.0 ^a	5
ch4	7.96	21.6 ^a	5
<i>Spitzer</i> /MIPS			
ch1	23.68	18.3 ^a	5

References: (1) archival data; (2) Hayashino et al. (2004); (3) Uchimoto et al. (2012); (4) Lawrence et al. (2007); (5) Hainline et al. (2009).

^a Median formal point-source sensitivity in the combined mosaic of 3σ (IRAC) and 5σ (MIPS).

Fig. 1, the area observed with IRAC and MIPS corresponds to about half the area of AzTEC/ASTE. The FWHMs of the PSF were 1.7, 1.7, 1.9, 2.0 and 6 arcsec, respectively. The source catalogues were generated in two ways. In the case of the MIPS $24\text{-}\mu\text{m}$ data, we extracted sources with $S/N \geq 5$ and measured the flux densities using the APEX module within the MOPEX (MOsaicker and Point source EXtractor) software package version 18.4.9 (Makovoz & Marleau 2005) through point-response function (PRF) fitting. For the IRAC data, we utilized SEXTRACTOR version 2.8.6 (Bertin & Arnouts 1996). We extracted sources that had at least five contiguous 0.6×0.6 arcsec² pixels with fluxes at least 1.5 times the background noise. Then flux densities were measured in 4.8-arcsec diameter apertures using the IRAF (version 2.14) task APPHOT. Sources at or above 3σ corresponding to their local noise were listed. The representative depth for each band is summarized in Table 4. The aperture corrections suggested in the IRAC Instrument Handbook were considered for all IRAC catalogues and the flux errors are expected to be within 10 per cent (Hainline et al. 2009).

3.3 Optical to near-infrared

Optical imaging observations with Subaru/Suprime-Cam (Miyazaki et al. 2002) using five broad-band filters (*B*, *V*, *R*, *i'* and *z'*) and one narrow-band filter (NB497) were obtained by Hayashino et al. (2004). We also utilized archival CFHT/MegaCam *U*-band data (P. I. L. Cowie) for the same area. Just 21 SMGs were also observed with Subaru/MOIRCS (Suzuki et al. 2008) in *J*, *H* and *Ks* bands (Uchimoto et al. 2008; Uchimoto et al. 2012). We made a set of photometry catalogues at these wavelengths utilizing SEXTRACTOR. We detected sources that had five connected pixels above the 2σ

noise level. The flux densities were measured with 2- and 1.1-arcsec diameter apertures for U , B , V , R , i' , z' bands and J , H , K_s bands respectively. We then cut the catalogues to $\geq 5\sigma$, as derived by Hayashino et al. (2004) and Uchimoto et al. (2008) and listed in Table 4. In addition, the archival J and K band Deep Extragalactic Survey (DXS) catalogues by UKIRT/Wide Field Camera (WFCAM; Lawrence et al. 2007) are available for all SMGs. These data are shallower than MOIRCS data, but valuable to us, since they can supplement the shortage of MOIRCS observations at near-infrared wavelengths.

4 COUNTERPART IDENTIFICATION

The majority of SMGs that were discovered by AzTEC/ASTE in the SSA22 field had no interferometric observations at submm/mm wavelengths. Only SSA22-AzTEC1 was observed with the Submillimeter Array (SMA; Tamura et al. 2010). In addition, SSA22-AzTEC12 and SSA22-AzTEC77 were confirmed with CO line emission (Chapman et al. 2005). Therefore, identifying counterparts in images taken at other wavelengths is an essential process in order to determine their accurate position and to investigate their nature. In this work we adopted the methods outlined by Downes et al. (1986) and Ivison et al. (2007) as well as some subsequent works (e.g. Wardlow et al. 2011; Biggs et al. 2011; Yun et al. 2012; Michałowski et al. 2012; Alberts et al. 2013). We utilized VLA 1.4-GHz, MIPS 24- μ m and IRAC 3.6-, 4.5-, 5.8- and 8.0- μ m imaging data. These data have better angular resolution than the AzTEC/ASTE survey. At the same time they are expected to detect SMGs with high probability. VLA 1.4-GHz reaches $\theta_{\text{FWHM}} \sim 3$ arcsec. It is well known that active star-forming galaxies radiate remarkable radio emission that reflects the degree of star formation activity (Condon 1992). MIPS 24- μ m is also suitable to detect SMGs and, while its angular resolution of $\theta_{\text{FWHM}} \sim 6$ arcsec is sometimes not enough to identify counterparts alone, it is significantly better than AzTEC/ASTE. Furthermore, Yun et al. (2008) suggested that SMGs always have a characteristic IRAC colour in the $([5.8 \mu\text{m}]/[3.6 \mu\text{m}])$ versus $([8.0 \mu\text{m}]/[4.5 \mu\text{m}])$ diagram and this idea is consistent with a small subset of SMGs observed by SMA. The IRAC observations achieve $\theta_{\text{FWHM}} \sim 2\text{--}4$ arcsec, corresponding to channels.

Sources that lie within a 2σ positional uncertainty, i.e. within a radius R_S from an AzTEC/ASTE centroid position, were extracted for each data set. R_S values were calculated as functions of S/N through Monte Carlo simulations (more details about this process are given in the Supplementary Information of Tamura et al. 2009 and Hatsukade et al. 2011). Then we calculated the corrected Poisson probability ($'p$ -value', hereafter p), the probability of chance association for all selected candidates. When calculating p , unlike most previous studies, we considered the number density of not just sources brighter than the candidate but all sources in each catalogue, as well as Yun et al. (2012), to avoid underestimating the p of nearby bright radio and/or mid-IR sources. In this article, we considered sources with $p \leq 0.05$ as robust counterparts. Likewise, we have also listed tentative sources ($0.05 < p \leq 0.20$). In calculating the source surface density, we faced a difficulty in the case of radio data. In order to estimate the p values, we must count what was detected as a source in the actual SSA22 map (i.e. not the real source density). However, terrible side lobes, which are caused by some bright radio objects located near this field, contaminated the 1.4-GHz radio image widely and we could only utilize some patchy regions that had low local noise levels, as mentioned in section 3.1. Thus, it was impossible to estimate source counts

for the whole region or for a significant wide submap. Therefore, we sampled small regions randomly across the map to estimate the radio source density. We generated 5000 circle regions having radii of 15 arcsec and counted radio sources within these regions. Contaminated areas that had local noise levels $> 20 \mu\text{Jy beam}^{-1}$ were excluded.

We found at least one robust counterpart for 19 AzTEC SMGs. We also found only tentative counterparts for an additional 40 AzTEC SMGs. The identified objects are listed in Table 5 and the finding charts for the 125 AzTEC SMGs are shown in Fig. 5 (and in the Supporting Information). The robust success rates of identifications based on VLA, MIPS and IRAC colour analysis were 11/66 (17 per cent), 11/64 (17 per cent) and 5/61 (8 per cent), respectively. An additional 10, 26 and 21 AzTEC sources have tentative VLA, MIPS and IRAC counterparts (Table 6). The tentative identification rates were 10/66 (15 per cent), 26/64 (39 per cent) and 21/61 (32 per cent), respectively. These rates are generally consistent with previous works for other fields. Among them, Yun et al. (2012) provide us with a proper opportunity to compare the results, since they also searched counterparts of 1.1-mm-selected SMGs discovered by AzTEC/ASTE in the GOODS-South field and utilized a similar identification method. Their robust (tentative) MIPS and IRAC colour identification rates of 8/48 (17 per cent; 14/48, 29 per cent) and 5/48 (10 per cent; 18/48, 32 per cent) agree with our studies. In the case of radio identification, their estimates of 13/48 (27 per cent) for robust sources and 19/48 (40 per cent) for tentative sources are slightly higher than our rates. The disparity could be caused by a difference in noise levels of the 1.4-GHz maps, since our radio map is noisier than their map. Indeed, Barger et al. (2012) reported that all 16 SMGs identified by SMA in a SCUBA-selected sample have radio counterparts utilizing the ultradeep ($1\sigma = 2.5 \mu\text{Jy}$) 1.4-GHz image obtained by the Karl G. Jansky Very Large Array (VLA). They found that 10 out of 16 SMGs have a relatively low radio flux density ($S_{1.4\text{GHz}} < 40 \mu\text{Jy}$). Therefore, surely we have missed such faint radio counterparts for a number of SMGs.

Recently, submm/mm interferometric observations targeting a number of SMGs have been carried out, providing us with the accuracy rate of these 'traditional methods'. Smolčić et al. (2012) made the Plateau de Bure Interferometer (PdBI) follow-up campaigns targeting 28 Atacama Pathfinder Experiment (APEX)/Large Apex Bolometer CAmera (LABOCA) selected SMGs in the COSMOS field and found that just about half of single-dish SMGs have real radio/IR-selected counterparts and > 10 per cent of SMGs should be comprised of multiple submm bright objects. ALMA observations of 90 SMGs in the CDF-S fields allow us to check answers using larger samples. They reveal that a number of predicted counterparts via radio and/or infrared images are identified by ALMA (~ 65 per cent), though about 40 per cent of single-dish SMGs have no such predictable counterpart (Hodge et al. 2013; Karim et al. 2013). While these results indicate that a statistical approach based on counterpart identification at wavelengths other than (sub-)millimetre is still meaningful, we should note that our counterpart catalogue cannot be perfectly correct. Additionally, it has also been reported that a portion of SMGs detected by single-dish telescopes are composed of multiple separated sources. For instance, Hodge et al. (2013) reported that 24 out of 69 SMGs detected by LABOCA are multiples based on their ALMA observations. Chen et al. (2013) showed that 3 out of 24 SMGs identified by SMA in a SCUBA-2 sample are multiples. Since the FWHM of the AzTEC/ASTE beam size (30 arcsec) is about 56 per cent larger than that of LABOCA (19.4 arcsec) and about twice that of SCUBA-2 (14 arcsec), multiplicity can be an important factor.

Table 5. Information about identified counterparts. The machine-readable version is available online. Robust counterparts are emphasized in bold face. (SSA22-Az77 was confirmed by CO detection: Chapman et al. 2005.) R_s represents the radius of the 2σ positional error circle estimated by Monte Carlo simulations. Dist. means the positional offset of counterparts from the AzTEC position. The *Spitzer* coordinate shows the coordinate of IRAC 3.6- μ m as priority. If counterparts were selected by MIPS alone, the MIPS 24- μ m coordinates are shown. The next three columns after the positional offset show p values of objects selected by VLA 1.4-GHz, *Spitzer* MIPS 24- μ m and IRAC colour-selected objects.

ID	R_s (arcsec)	Radio coordinate (J2000)	Dist. (arcsec)	<i>Spitzer</i> coordinate (J2000)	Dist. (arcsec)	$p_{1.4\text{ GHz}}$	$p_{24\ \mu\text{m}}$	p_{colour}
SSA22-Az1a	3.7	J221732.41+001743.9	3.3	J221732.42+001743.8	3.4	0.010	...	0.042
SSA22-Az2a	5.1	J221742.26+001701.2	2.6	J221742.25+001701.8	2.5	0.011	0.007	0.045
SSA22-Az5a	5.7	J221718.65+001802.7	4.2	J221718.67+001803.1	4.0	0.020	0.02	0.082
SSA22-Az6a	6.0	J221815.41+000946.3	3.2	0.068
SSA22-Az9a	6.7	J221659.92+001039.0	2.5	0.013
SSA22-Az11a	7.2	J221657.33+001923.9	1.3	0.023
SSA22-Az12a	7.3	J221734.03+001347.5	4.1	...	0.028	0.106
SSA22-Az12b	7.3	J221733.92+001352.2	6.8	J221733.96+001351.9	6.2	0.037	...	0.146
SSA22-Az13a	7.5	J221720.25+002019.0	3.3	0.085
SSA22-Az14a	7.5	J221737.02+001821.5	0.9	...	0.008	0.013
SSA22-Az14b	7.5	J221737.22+001816.6	6.0	0.149
SSA22-Az14c	7.5	J221737.33+001822.9	5.6	0.034
SSA22-Az16a	7.8	J221651.98+001816.9	6.0	...	0.042	...
SSA22-Az18a	8.1	J221742.10+001246.4	7.7	0.182
SSA22-Az20a	8.4	J221744.06+000822.8	2.1	J221744.08+000822.7	1.8	0.011	...	0.042
SSA22-Az20b	8.4	J221744.30+000821.9	1.8	0.042
SSA22-Az23a	8.7	J221658.21+002452.7	6.3	0.180
SSA22-Az23b	8.7	J221658.08+002457.4	5.3	0.158
SSA22-Az23c	8.7	J221658.22+002458.1	7.3	0.197
SSA22-Az26a	9.0	J221712.99+002654.1	6.0	0.182
SSA22-Az27a	9.0	J221825.31+001924.8	1.3	...	0.007	...
SSA22-Az28a	9.1	J221650.06+002248.6	3.6	0.108
SSA22-Az30a	9.2	J221746.77+000804.2	6.2	0.047
SSA22-Az31a	9.3	J221727.39+000317.6	8.9	...	0.061	0.236
SSA22-Az32a	9.4	J221804.95+000840.1	4.7	0.150
SSA22-Az32b	9.4	J221805.26+000839.4	2.4	0.065
SSA22-Az34a	9.5	J221741.34+002641.4	2.9	...	0.025	0.086
SSA22-Az34b	9.5	J221741.78+002639.4	7.7	0.057
SSA22-Az35a	9.6	J221741.27+001045.9	5.4	...	0.042	0.175
SSA22-Az35b	9.6	J221741.44+001045.1	3.0	J221741.30+001045.6	4.8	0.021	0.042	...
SSA22-Az37a	9.9	J221737.39+001024.8	7.1	J221737.39+001024.9	7.1	0.057	0.064	0.224
SSA22-Az45a	10.7	J221732.29+002931.3	6.3	J221732.33+002930.6	5.4	0.056	...	0.191
SSA22-Az50a	11.1	J221720.83+002826.1	4.8	0.172
SSA22-Az52a	11.2	J221728.32+002025.9	10.8	J221728.37+002027.0	9.8	0.084	...	0.307
SSA22-Az52b	11.2	J221728.99+002033.6	3.5	0.117
SSA22-Az55a	11.5	J221806.46+001135.4	9.5	...	0.094	0.314
SSA22-Az56a	11.8	J221806.23+001021.0	1.2	0.025
SSA22-Az59a	12.0	J221814.32+001446.3	4.0	...	0.040	...
SSA22-Az59b	12.0	J221815.13+001445.4	9.3	...	0.096	...
SSA22-Az65a	12.3	J221801.22+002928.4	5.5	...	0.059	...
SSA22-Az67a	12.3	J221707.63+001307.6	10.6	...	0.110	0.353
SSA22-Az67b	12.3	J221707.21+001312.9	5.1	...	0.065	0.199
SSA22-Az67c	12.3	J221708.10+001323.2	12.0	...	0.111	...
SSA22-Az68a	12.3	J221812.90+002321.4	7.6	...	0.085	...
SSA22-Az71a	12.4	J221723.13+000926.2	7.8	...	0.087	...
SSA22-Az72a	12.5	J221728.20+002851.4	4.9	J221728.22+002851.7	5.2	0.047	0.067	0.203
SSA22-Az74a	12.5	J221706.61+001727.7	8.2	...	0.093	0.310
SSA22-Az75a	12.5	J221724.47+000731.7	9.1	...	0.106	0.332
SSA22-Az75b	12.5	J221724.45+000717.5	6.9	...	0.078	...
SSA22-Az75c	12.5	J221723.79+000714.0	11.4	...	0.113	...
SSA22-Az77a	12.8	J221735.15+001537.4	4.6	0.180
SSA22-Az77b	12.8	J221734.99+001535.2	4.4	...	0.046	...
SSA22-Az77c	12.8	J221734.98+001527.4	12.0	...	0.119	...
SSA22-Az80a	12.9	J221713.07+001918.9	11.8	...	0.116	0.388
SSA22-Az80b	12.9	J221713.35+001936.6	10.0	...	0.117	0.361
SSA22-Az81a	12.9	J221702.29+001550.4	8.4	...	0.085	0.323
SSA22-Az81b	12.9	J221702.35+001611.1	12.7	...	0.118	0.398
SSA22-Az83a	13.0	J221657.28+002409.6	3.9	0.148

Table 5 – *continued*

ID	R_s (arcsec)	Radio coordinate (J2000)	Dist. (arcsec)	<i>Spitzer</i> coordinate (J2000)	Dist. (arcsec)	$p_{1.4\text{GHz}}$	$p_{24\ \mu\text{m}}$	p_{colour}
SSA22-Az108a	13.8	J221736.48+002219.8	8.1	...	0.099	...
SSA22-Az109a	13.9	J221826.18+002028.6	10.0	0.109
SSA22-Az110a	13.9	J221750.48+001509.3	8.1	J221750.51+001509.4	7.6	0.090	...	0.318
SSA22-Az113a	14.1	J221747.60+002318.3	11.5	...	0.132	0.419
SSA22-Az113b	14.1	J221748.43+002316.6	1.4	...	0.009	...
SSA22-Az115a	14.2	J221705.39+001514.0	12.0	...	0.145	0.431
SSA22-Az116a	14.2	J221720.22+001552.9	11.4	...	0.134	...
SSA22-Az116b	14.2	J221719.34+001545.1	7.0	...	0.088	...
SSA22-Az117a	14.2	J221732.15+002540.4	8.3	...	0.127	0.346
SSA22-Az84a	13.1	J221819.43+002126.6	5.7	0.058
SSA22-Az85a	13.1	J221816.06+002452.6	10.7	0.106
SSA22-Az85b	13.1	J221816.67+002452.1	4.8	...	0.052	...
SSA22-Az87a	13.2	J221726.02+002026.7	8.6	...	0.111	0.335
SSA22-Az88a	13.2	J221804.43+002153.2	0.9	J221804.49+002153.3	1.5	0.004	0.009	...
SSA22-Az91a	13.4	J221736.64+000343.4	4.2	0.165
SSA22-Az95a	13.5	J221736.74+000820.9	5.0	J221736.72+000820.9	5.3	0.051	0.077	0.218
SSA22-Az96a	13.5	J221754.66+001923.3	10.0	...	0.121	0.375
SSA22-Az98a	13.5	J221811.25+001656.8	9.2	...	0.109	...
SSA22-Az99a	13.5	J221725.38+001803.9	7.8	...	0.107	0.317
SSA22-Az99b	13.5	J221725.18+001805.8	9.0	...	0.107	0.351
SSA22-Az99c	13.5	J221724.63+001807.9	13.4	...	0.133	...
SSA22-Az101a	13.6	J221756.36+002812.9	4.8	...	0.054	...
SSA22-Az102a	13.6	J221744.48+000632.4	2.2	0.068
SSA22-Az103a	13.7	J221801.84+000744.8	4.7	0.191
SSA22-Az106a	13.7	J221723.70+001652.4	12.8	J221723.70+001652.4	12.8	0.123	0.136	0.428

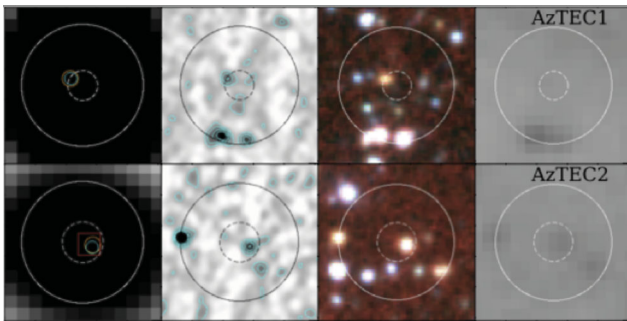


Figure 5. Finding charts for the SMGs discovered by AzTEC/ASTE in the SSA22 field. The full chart is available online. In addition to the AzTEC 1.1-mm images, images from VLA 1.4-GHz, IRAC false colour and 24- μm are shown from left to right. Blank or partly lacking images indicate that these SMGs were not observed at the corresponding wavelengths. The solid and dashed circles show the representative FWHM of AzTEC/ASTE (diameter is 30 arcsec) and 2σ positional error circle. The IRAC colour images are produced using the 3.6- μm (blue), 4.5- μm (green) and 5.8- μm (red) band images. Each image is $40 \times 40 \text{ arcsec}^2$ in size. The identified counterparts are shown in the left figure. Cyan circles mark the 1.4-GHz radio sources and red squares are the MIPS 24- μm sources, while IRAC sources are represented by orange circles.

5 PHOTOMETRIC REDSHIFT

For all AzTEC SMGs in the SSA22 field, spectroscopic redshifts, z_{spec} , are available for only a small subset (5/125, 4 per cent). Here we estimate photometric redshifts of reliable (i.e. both robust and tentative) SMG counterparts to derive the redshift distribution and extract candidate SMGs that lie within the $z = 3.1$ protocluster. Chapman et al. (2005) reported that there were 10 SCUBA SMGs

Table 6. SMG identification statistics. The number of SMGs having counterparts are listed. Combining the three data sets, eventually 59 SMGs have at least one counterpart. SMGs with photo- z are composed of IRAC counterparts and VLA/MIPS counterparts covered by IRAC (i.e. some of them do not have good p in the case of IRAC). Two SMGs (SSA22-AzTEC71 and SSA22-AzTEC108) have MIPS counterparts, but we cannot find corresponding IRAC sources.

Class	Number	Percentage (%)
Total detected SMGs ($S/N \geq 3.5$)	125	
SMGs with any of the counterparts	59	
SMGs covered by VLA	66/125	53
(with robust VLA counterparts)	11/66	17
(with tentative VLA counterparts)	10/66	15
SMGs covered by MIPS	64/125	51
(with robust MIPS counterparts)	11/64	17
(with tentative MIPS counterparts)	26/64	39
SMGs covered by IRAC	61/125	49
(with robust IRAC counterparts)	5/61	8
(with tentative IRAC counterparts)	31/61	51
(with photo- z)	45/61	74
(without any counterpart)	14/61	23

that have spectroscopic redshifts in this field. However, only 3 out of 10 sources were detected in the AzTEC map with S/N of ≥ 3.5 . The origin of this inconsistency is still unclear, but incompleteness in the AzTEC map might account for this difference. Indeed, most of these sources significantly detected by SCUBA are marginally detected with the AzTEC/ASTE survey ($2.5 < S/N < 3.5$). Hereafter we mainly focus on AzTEC SMGs.)

Table 7. Redshifts of identified counterparts. Derived photometric redshifts, z_p , with 68 per cent confidence intervals based on optical to near-infrared data are shown. The next column stands for spectroscopic redshifts, z_s . The third column, z_p (mm/radio), is for photometric redshifts with 68 per cent confidence intervals evaluated using 1.1-mm and radio fluxes. (We had not calculated redshifts for SSA22-Az106a and SSA22-Az110a, as these were clearly radio-loud AGN and it was difficult to apply the code.)

ID	z_p	z_s	z_p (mm/radio)	ID	z_p	z_s	z_p (mm/radio)
SSA22-Az1a	$2.85^{+3.15}_{-0.98}$ ^a	...	$1.7^{+1.8}_{-0.8}$	SSA22-Az56a	$0.95^{+0.07}_{-0.07}$
SSA22-Az2a	$2.15^{+0.23}_{-0.21}$	2.278^b	$2.1^{+1.4}_{-1.2}$	SSA22-Az67a	$1.70^{+1.04}_{-0.30}$
SSA22-Az5a	$3.00^{+1.27}_{-1.67}$...	$1.7^{+1.8}_{-1.0}$	SSA22-Az67b	$1.45^{+0.30}_{-0.11}$
SSA22-Az6a	$2.40^{+3.60}_{-0.82}$	SSA22-Az72a	$4.10^{+0.15}_{-0.26}$...	$2.0^{+1.5}_{-1.1}$
SSA22-Az9a	$2.0^{+3.5}_{-0.9}$	SSA22-Az74a	$0.95^{+0.12}_{-0.20}$
SSA22-Az11a	$2.55^{+3.45}_{-0.69}$	SSA22-Az75a	$1.10^{+0.26}_{-0.17}$
SSA22-Az12a	$1.90^{+0.26}_{-0.35}$	SSA22-Az75c	$0.65^{+0.16}_{-0.07}$
SSA22-Az12b	$2.20^{+0.72}_{-0.32}$	2.555^c	$2.0^{+1.6}_{-1.0}$	SSA22-Az77a	$2.80^{+0.37}_{-0.34}$	3.098^c	...
SSA22-Az13a	$2.15^{+0.55}_{-0.16}$	3.11^d	...	SSA22-Az77c	$2.55^{+0.18}_{-0.20}$
SSA22-Az14a	$2.90^{+0.21}_{-0.32}$	SSA22-Az80a	$0.40^{+0.05}_{-0.06}$
SSA22-Az14b	$2.00^{+0.20}_{-0.29}$	SSA22-Az80b	$2.90^{+0.24}_{-0.54}$
SSA22-Az14c	$3.70^{+0.72}_{-0.19}$...	$1.8^{+2.2}_{-0.9}$	SSA22-Az81a	$2.05^{+0.32}_{-0.20}$
SSA22-Az18a	$6.00^{+0.00}_{-4.06}$	SSA22-Az81b	$0.45^{+0.03}_{-0.05}$
SSA22-Az20a	$2.25^{+0.20}_{-0.40}$...	$2.0^{+3.2}_{-0.5}$	SSA22-Az83a	$2.55^{+0.09}_{-0.10}$
SSA22-Az20b	$3.75^{+0.21}_{-0.72}$	SSA22-Az84a	$1.8^{+1.3}_{-1.3}$
SSA22-Az23a	$6.00^{+0.00}_{-4.18}$	SSA22-Az85a	$2.1^{+1.4}_{-1.2}$
SSA22-Az23b	$1.25^{+0.70}_{-0.11}$	SSA22-Az87a	$1.80^{+0.44}_{-0.47}$
SSA22-Az23c	$2.35^{+2.32}_{-1.41}$	SSA22-Az88a	$1.9^{+1.6}_{-1.1}$
SSA22-Az26a	$1.05^{+0.12}_{-0.08}$	SSA22-Az91a	$2.10^{+3.42}_{-0.53}$
SSA22-Az28a	$0.00^{+0.01}_{-0.00}$	SSA22-Az95a	$6.00^{+0.00}_{-0.68}$...	$2.0^{+1.2}_{-1.5}$
SSA22-Az30a	$1.8^{+1.2}_{-1.3}$	SSA22-Az96a	$2.55^{+0.08}_{-0.20}$
SSA22-Az31a	$2.35^{+2.59}_{-1.18}$	SSA22-Az99a	$1.90^{+0.17}_{-0.35}$
SSA22-Az32a	$2.25^{+3.75}_{-0.91}$	SSA22-Az99b	$2.25^{+0.84}_{-0.30}$
SSA22-Az32b	$0.85^{+0.05}_{-0.07}$	SSA22-Az102a	$0.65^{+0.08}_{-0.07}$
SSA22-Az34a	$3.30^{+0.19}_{-0.21}$...	$1.9^{+1.8}_{-0.9}$	SSA22-Az103a	$1.95^{+0.04}_{-0.04}$
SSA22-Az35a	$0.35^{+0.10}_{-0.06}$	SSA22-Az106a	$0.45^{+0.04}_{-0.05}$...	—
SSA22-Az35b	$1.7^{+1.5}_{-0.5}$	SSA22-Az108a	$2.40^{+0.20}_{-0.95}$
SSA22-Az37a	$2.20^{+0.18}_{-0.25}$	2.614^c	$1.9^{+1.2}_{-1.4}$	SSA22-Az109a	$2.0^{+1.5}_{-1.5}$
SSA22-Az45a	$1.75^{+4.25}_{-0.82}$...	$2.1^{+1.7}_{-1.1}$	SSA22-Az110a	$2.75^{+2.75}_{-0.80}$...	—
SSA22-Az50a	$1.95^{+0.37}_{-0.07}$	SSA22-Az113b	$1.20^{+0.06}_{-0.09}$
SSA22-Az52a	$1.9^{+1.7}_{-0.9}$	SSA22-Az115a	$2.80^{+0.07}_{-0.03}$
SSA22-Az52b	$2.85^{+2.70}_{-0.69}$	SSA22-Az116a	$4.70^{+0.24}_{-0.19}$
SSA22-Az55a	$2.20^{+0.06}_{-0.05}$	SSA22-Az117a	$1.30^{+0.11}_{-0.26}$

References:

^a $z_p = 3.19^{+0.26}_{-0.35}$ in Tamura et al. (2010).

^bAlaghband-Zadeh et al. (2012).

^cChapman et al. (2005).

^dMatsuda et al. (2005).

For radio counterparts, their photometric redshifts based on 1.1-mm and radio fluxes were estimated with a Bayesian technique (Aretxaga et al. 2007). The results are summarized in Table 7. Derived redshifts were not restricted very much and therefore we mainly discuss redshifts of counterparts based on optical to near-infrared photometries.

5.1 SED fitting

We performed SED fitting and obtained photometric redshifts using the HYPERZ version 1.1 code (Bolzonella, Miralles & Pelló 2000). As

shown in Fig. 1, the imaging area does not cover the AzTEC map completely and a significant number of SMGs do not have complete photometric data. This constraint forced us to consider only the area observed by all IRAC channels when deriving photometric redshifts, since these wavelength data are essential to observe characteristic features such as the 1.6- μ m bump, which is caused by a minimum in the opacity of the negative hydrogen ion in the atmospheres of cool stars (Sorba & Sawicki 2010), and to obtain well-restricted redshift information. It is also difficult to derive photometric redshifts for some radio and/or MIPS counterparts that had no IRAC component.

Among these 61 SMGs, 14 SMGs have no reliable counterpart when considering all three identification methods. Two SMGs have MIPS counterparts, but we cannot find corresponding IRAC sources with red colour. Therefore the fitting analysis was performed for the remaining 45 SMGs. Photometric catalogues for U (CFHT), B , V , R , i' , z' bands (Subaru/Suprime-Cam), J , H , K_s bands (Subaru/MOIRCS) and 3.6, 4.5, 5.8, 8.0 μm (*Spitzer*/IRAC) were considered, while the J , K (UKIRT) catalogues were utilized only for sources that were not observed by MOIRCS. We matched the counterpart catalogue with the optical to near-infrared catalogues, using a search radius of $r = 1.2$ arcsec. In fitting SEDs, the following parameters were considered. The range of redshift was set to 0–6. Dust extinction is considered with a range of $A_v = 0$ –5 mag using a bin of 0.5 and we adopted the model of Calzetti et al. (2000). Bruzual & Charlot (1993) SED templates of elliptical, Sb, burst, constant and star-formation (Im) are utilized.

5.2 Results

We summarize the derived photometric redshifts in Table 7. The comparison of spectroscopic and photometric redshifts for SMG counterparts is shown in Fig. 6. A majority of sources, except for Az13a, have comparatively small relative errors. Only Az13a has a catastrophic error (i.e. $|z_{\text{photo}} - z_{\text{spec}}|/(1 + z_{\text{spec}})$ of >0.15 ; e.g. Ilbert et al. 2009). This source is bright in the X-ray and is supposed to harbour an AGN. Thus, as a whole, the photometric redshifts are consistent with the spectroscopic redshifts, though only five (candidate) counterparts have spectroscopic redshifts.

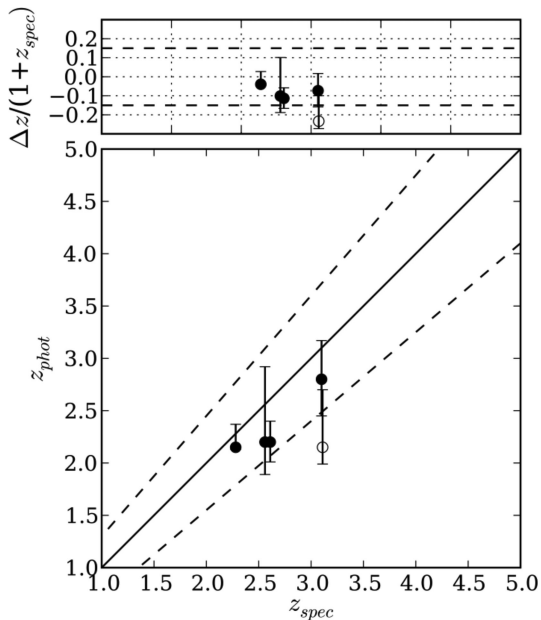


Figure 6. Photometric redshifts versus the spectroscopic redshifts from previous works (Matsuda et al. 2005; Chapman et al. 2005; Alaghband-Zadeh et al. 2012). The error bars correspond to a 1σ confidence range. The dashed lines represent $z_{\text{phot}} = z_{\text{spec}} \pm 0.15(1 + z_{\text{spec}})$. Filled circles show sources that were identified as SMGs. The open circles represent SSA22-Az13a, which has a spectroscopic redshift of 3.1 but is only the most reliable of the tentative counterparts of SSA22-AzTEC13 (see Section 5.2). The upper panel shows the errors of $(z_{\text{phot}} - z_{\text{spec}})/(1 + z_{\text{spec}})$. One outlier at $z = 3.1$, SSA22-Az13a, is an X-ray source and should be an active galactic nucleus host (Lehmer et al. 2009, Tamura et al. 2010).

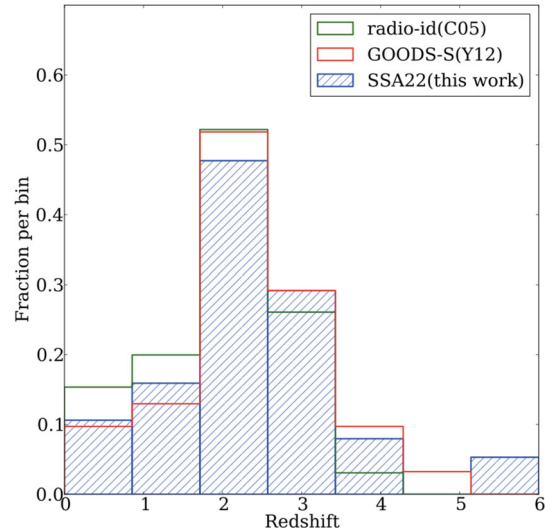


Figure 7. Redshift distribution of AzTEC SMGs in the SSA22 field based on photometric/spectroscopic redshifts. 48 counterpart candidates were considered and $z_{\text{med}} = 2.4$. For comparison, we include 36 AzTEC SMGs with optical photometric redshifts (Yun et al. 2012) and 76 radio-identified SCUBA SMGs with spectroscopic redshifts (Chapman et al. 2005).

Fig. 7 represents the redshift distribution of 48 counterparts of 45 AzTEC SMGs in the SSA22 field. All robust counterparts that have photometric or spectroscopic redshifts were considered. Three SMGs have two robust counterparts and we utilized both in such cases. For SMGs that have only tentative counterparts, we selected the most reliable counterpart, i.e. the one with the best p_{color} value. In calculating the distribution of redshifts, the spectroscopic redshifts were considered when provided by the sources. In the case of SSA22-AzTEC1a, we adopted the photometric redshift using mid- and far-infrared data (Tamura et al. 2010). For the remaining sources without spectroscopic redshifts, we considered photometric redshifts. In the same figure, two redshift distributions, obtained previously based on optical to near-infrared data, are also shown. One is the SCUBA SMGs that were identified by radio imaging and have spectroscopic redshifts (Chapman et al. 2005) and the other is composed of AzTEC SMGs in the GOODS-S field with optical photometric redshifts (Yun et al. 2012).

We derived a median redshift of $z_{\text{med}} = 2.4$ for AzTEC SMGs in the SSA22 field. It is likely that the distribution of AzTEC SMGs in the SSA22 fields is similar to the ones in the previous two works, though the peak of the distribution is slightly higher than both the SCUBA sources and AzTEC SMGs in GOODS-S. The shift can be explained reasonably by considering that longer-wavelength surveys are at an advantage in detecting higher redshift SMGs and that the SCUBA SMGs reported in Chapman et al. (2005) were composed of radio sources only. Likewise, Smolčić et al. (2012) reported more reliable statistics of interferometrically identified SMGs. They performed a 1.3-mm continuum survey with PdBI of 1.1-mm-selected SMGs and derived the redshift distribution of these identified counterparts (their redshifts are also generally derived from optical photometry). The median redshift of 1.1-mm-selected SMGs with photometric redshifts (i.e. not lower limits) is $z_{\text{med}} = 2.5$, which is consistent with our work. However, we should note that these distributions might not represent the whole redshift distribution of AzTEC SMGs. It is found that 14 out of 61 SMGs with four-band IRAC coverage (23 per cent) have no reliable

counterparts for all diagnostics, which prevents us from estimating their redshifts completely. Some of the SMGs are possibly too faint to detect at such wavelengths, since they are at higher redshift ($z \geq 4$).

6 LARGE-SCALE STRUCTURE

In the SSA22 field, AzTEC/ASTE covered the area where the large-scale structure traced by $z = 3.1$ LAEs was discovered by Hayashino et al. (2004). It is expected that a certain fraction of our SMGs found towards the high-density region of LAEs can reside within the large-scale structure. Our estimate of the photometric redshifts allows us to extract candidate SMGs at $z = 3.1$ and to investigate the relationship between SMGs and the large-scale structure.

Combining our estimate of the photometric redshifts with spectroscopic and photometric redshifts from the literature, the following 10 AzTEC SMGs are listed as cluster member candidates. First, it has been reported that two SMGs should be at $z = 3.1$. Az77a was also detected by the SCUBA survey (SMM J221735.15+001537.2). It had CO detection and $z_{\text{spec}} = 3.098$ (Chapman et al. 2005). An SMA follow-up observation revealed that Az1a is the real counterpart of SSA22-AzTEC1. Tamura et al. (2010) estimated its redshift as $z_{\text{phot}} = 3.19^{+0.26}_{-0.35}$, based on SED fitting in the mid-infrared to radio wavelength range. Secondly, Az13a is not only an IRAC red object but also a Lyman α emitter with a spectroscopic redshift of $z_{\text{spec}} = 3.11$ (Matsuda et al. 2005). Thirdly, we extract seven sources that could be at $z = 3.1$ based on photometric redshifts. The uncertainty in the photometric redshifts at $z \simeq 3$ was estimated as $\Delta z \leq 0.5$ in the case of our data set (Uchimoto et al. 2012) and therefore we listed Az5a, Az14a, Az34a, Az52b, Az80b, Az110a and Az115a, since they have the most reliable photometric redshifts in the range $z_{\text{phot}} = 3.1 \pm 0.5$. Here we exclude sources that were

detected in IRAC channels only (i.e. too faint in the optical range), since we cannot derive well-defined photometric redshifts in such cases.

6.1 Sky distribution

Fig. 8 shows the two-dimensional distribution of the $z = 3.1$ candidate SMGs compared with the surface density distribution of LAEs at $z = 3.1$ (Hayashino et al. 2004). The area shown in Fig. 8 corresponds to a field of view of Suprime-Cam that was denoted ‘sb1’ in Yamada et al. (2012). As is evident from this figure, the $z = 3.1$ candidate SMGs are concentrated into the overdense region, while the other SMGs are uniformly distributed across the area observed by IRAC. In particular, seven SMGs are concentrated in the ‘core’ region (shown in Fig. 8) within the central $12 \text{ Mpc} \times 12 \text{ Mpc}$ (comoving), which is the most overdense region of LAEs.

It has also been reported that the density peak of the K -band selected (K -selected) galaxies ($K_{AB} < 24$) at $2.6 < z_{\text{phot}} < 3.6$ is consistent with that of LAEs (Kubo et al. 2013). This supports the idea that these SMGs are at the centre of the protocluster. They also found both dusty star-forming galaxies and quiescent galaxies around the ‘core’ region. The high source surface density of dusty K -selected galaxies within the region supports the reality of the structure traced by SMGs and also implies high star-forming activity in this overdense region.

As shown in Fig. 8, the ‘core’ region roughly corresponds to the area named as SSA22a in Steidel et al. (2000). Yamada et al. (2012) calculated the degree of overdensity of LAEs for sb1 and SSA22a and furthermore estimated the underlying mass fluctuation assuming the standard Λ CDM model for both regions. They concluded that 10 and 19 times the average mass fluctuation was derived, respectively. Hence SMGs are likely to concentrate in an area where

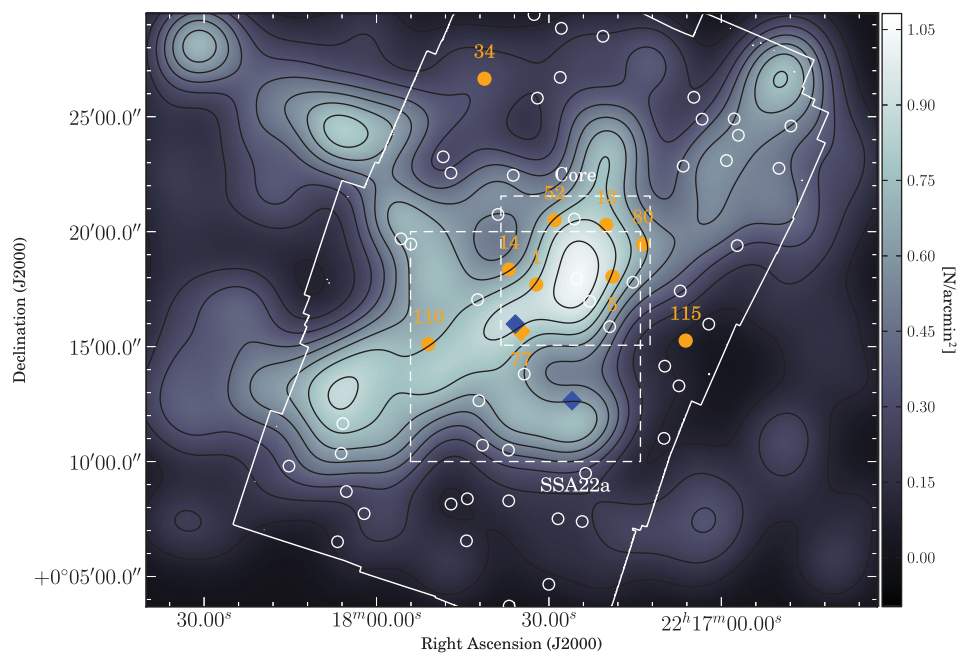


Figure 8. Sky distribution of the $z = 3.1$ candidate SMGs and the large-scale structure traced by LAEs at $z = 3.1$. The background map shows the density distribution of $z = 3.1$ LAEs (Hayashino et al. 2004). The contours show the smoothed densities of 0.12, 0.23, 0.35, 0.46, 0.57, 0.69, 0.81 and 0.92 galaxies per arcmin². Superposed orange diamonds (circles) show the $z = 3.1$ (candidate) AzTEC SMGs. Diamonds are SCUBA SMGs that lie at $z = 3.1$. The two SCUBA SMGs with blue diamonds were not detected in the AzTEC map ($S/N < 3.5$). SSA22-AzTEC77 was detected by both AzTEC and SCUBA and therefore is shown as the orange diamond. The white solid line stands for the area of IRAC ch1 observations. White circles denote the remaining AzTEC SMGs located within the IRAC area. Seven out of 10 $z \sim 3.1$ AzTEC SMGs are concentrated in the core region within a $12 \text{ Mpc} \times 12 \text{ Mpc}$ square (comoving scale). For reference, we also show the area ‘SSA22a’, named by Steidel et al. (2000).

the underlying mass fluctuation is significantly high. Note that this spatial correlation between LAEs and SMGs could not occur accidentally. When 10 sources are randomly scattered in the IRAC field, the probability that more than three sources are located within the core region is $\ll 1$ per cent.

Regarding the extent of SMGs, there is an intriguing work by Michałowski et al. (2012) that reported that there is a clear inconsistency between the redshift distributions of SMGs in the Lockman Hole and UDS fields. They insisted that the large-scale structures in the $z = 0\text{--}5$ Universe extending from ~ 0.3 to 0.7 deg could explain the difference reasonably. The extent of the area shown in Fig. 8 is ~ 0.5 deg, which corresponds to ~ 50 Mpc at $z = 3.1$. Therefore our results generally agree with theirs and indicate that the distribution of SMGs could be patchier than their estimate, at least at $z \sim 3$.

6.2 Cross-correlation function

As mentioned above, the sky distribution of the $z = 3.1$ candidate SMGs suggests that a majority of SMGs are located in the most overdense region at the dozens-of-Mpc scale and that some SMGs lie in relatively less overdense regions. The two-point angular cross-correlation function is useful to evaluate statistically the degree of similarity in distributions between two types of galaxies, in this case SMGs and LAEs. We calculate it in a way similar to the one used in Tamura et al. (2009), described only briefly here. The angular distances for all pairs between the two populations are measured and the incremental quantity within a unit solid angle as a function of angular distance is calculated. At this time, the estimator equation proposed by Landy & Szalay (1993) is utilized. We confine the area so as not to generate artificial positive signals. Hereafter, we will consider the field observed by IRAC (see Fig. 7). Moreover, pairs separated by more than 15 arcsec are excluded to avoid the source confusion effect.

The computed angular cross-correlation function between 10 $z \sim 3.1$ SMGs and 195 $z = 3.1$ LAEs is shown in Fig. 9. For comparison, the auto-correlation function of LAEs is also shown. Error bars for the correlation functions were estimated from the r.m.s. of 5000 bootstrap samples of the original catalogues. Our results suggest that $z \sim 3.1$ SMGs are clustered and that their distribution

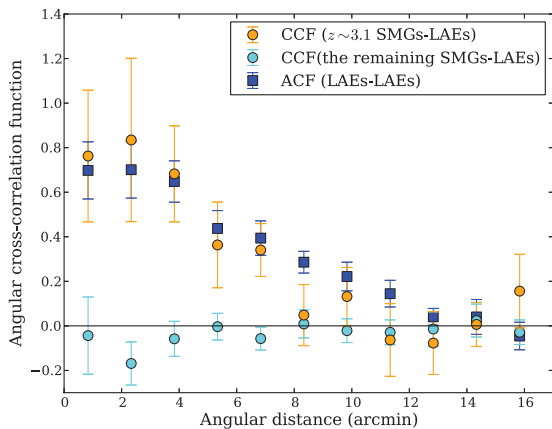


Figure 9. The two-point angular cross-correlation functions of SSA22 galaxies. The orange circles represent the cross-correlation functions of LAEs and $z = 3.1$ SMG candidates. Blue squares show the auto-correlation functions of LAEs. These results indicate that the distributions of selected SMGs are correlated with those of $z = 3.1$ LAEs. For comparison, the cross-correlation functions of LAEs and the remaining 51 SMGs are also shown using cyan circles.

is similar to that of $z = 3.1$ LAEs, since we find positive amplitudes for the cross-correlation at angular distances ≤ 7 arcmin. We also computed the cross-correlation function between the remaining 51 SMGs covered by IRAC and the $z = 3.1$ LAEs in similar fashion. In this case, it is suggested that the distributions of the two are not correlated. The correlation between SMGs and LAEs in SSA22 was first shown in Tamura et al. (2009). Though their selection of SMGs was based only on luminosity, they showed a possible correlation between the two samples. Our work confirms the trend that they reported, constraining the photometric redshifts. Consequently, we arrive at a more sophisticated understanding of the correlation: the amplitude of the function is higher and the significance of the correlations is increased.

A similar approach using cosmological hydrodynamics simulations was followed by Shimizu, Yoshida & Okamoto (2012). They also calculated the cross-correlation function focusing on the $z = 3.1$ Universe in their simulation box, utilizing a code that successfully reproduced the observed source counts of SMGs. They indicated two trends. First, they reported that there is a correlation between the distributions of SMGs and LAEs. Therefore, as a whole, our results are consistent with their simulations and suggest that SMGs selectively reside in relatively massive dark matter haloes. The second trend is that the cross-correlation function between SMGs and LAEs has a profile similar to that of the correlation function between SMGs and dark matter haloes, as presented in previous works (e.g. Suwa, Hirashita & Tamura 2010). The observed amplitudes of the cross-correlation function of SMGs and LAEs are, however, much higher than that predicted from the simulation. The reason is not apparent, but one possible interpretation is that, in the SSA22 field, the degree of mass assembly is much larger than was assumed in the simulation and as a consequence the degree of clustering of galaxies becomes higher.

7 SUMMARY

We imaged a 950-arcmin^2 field towards the SSA22 field, covering a 1σ depth down to $0.7\text{--}1.3$ mJy, using the AzTEC 1.1-mm camera attached to the ASTE. This survey area corresponds to about 2.5 times the area previously reported (390 arcmin^2) by Tamura et al. (2009). We detected 125 SMGs with $S/N \geq 3.5$; eight of these are expected to be fake sources arising from noise peaks.

We attempted to identify reliable counterparts to 125 AzTEC SMGs utilizing VLA 1.4-GHz imaging, MIPS 24- μm images and IRAC colour diagnostics (Yun et al. 2008). We considered the corrected Poissonian probability, p , to evaluate the degree of chance coincidence. We regarded counterpart candidates as robust counterparts if p is less than 0.05. Additionally, sources with $0.05 \leq p < 0.20$ were considered as tentative counterparts. We found that 59 SMGs have at least one reliable (i.e. robust or tentative) counterpart, considering all diagnostics methods.

We performed SED fitting based on optical to near-infrared photometry utilizing the HYPERZ code, which provided us with photometric redshifts for 48 counterparts of 45 SMGs, all covered by all-band IRAC observations. We could not find any counterparts for 14 of 61 SMGs that had four-band IRAC coverage. The redshift distribution of the SSA22 field is similar to those of GOODS-S AzTEC SMGs reported by Yun et al. (2012). These AzTEC SMGs tend to lie in a higher redshift Universe than the radio-identified SCUBA SMGs ($z_{\text{med}} = 2.2$ reported by Chapman et al. 2005). Some AzTEC sources without reliable counterparts may be located at higher z and would enhance this trend.

We found 10 AzTEC SMGs that are possibly at $z = 3.1$ based on photometric and/or spectroscopic redshifts. Among them, seven out of the 10 SMGs were concentrated into the core $12 \text{ Mpc} \times 12 \text{ Mpc}$ region (comoving scale), which is consistent with the centre of the galaxy distribution of the protocluster. Cross-correlation functions indicate that the distribution of these 10 SMGs and that of $z = 3.1$ LAEs are correlated. These results suggest that SMGs tend to be formed in extremely high-density environments.

ACKNOWLEDGEMENTS

The ASTE project is driven by Nobeyama Radio Observatory (NRO), a branch of NAOJ, in collaboration with the University of Chile and Japanese institutes including the University of Tokyo, Nagoya University, Osaka Prefecture University, Ibaraki University and Hokkaido University. Observations with ASTE were in part carried out remotely from Japan using NTT's GEMnet2 and its partner R&E (Research and Education) networks, which are based on the AccessNova collaboration of the University of Chile, NTT Laboratories and NAOJ. AzTEC analysis performed at UMass is supported in part by NSF grant 0907952. This study was supported by the MEXT Grant-in-Aid for Specially Promoted Research (no. 20001003) and the Grant-in-Aid for the Scientific Research from the Japan Society for the Promotion of Science (no. 19403005). This article is based on data collected at Subaru Telescope, which is operated by the National Astronomical Observatory of Japan. This work is based on observations made with the *Spitzer* Space Telescope, which is operated by the Jet Propulsion Laboratory, California Institute of Technology under a contract with NASA. Some of the data reported here were obtained as part of the UKIRT Service Programme. SI is financially supported by a Research Fellowship from the JSPS for Young Scientists. YT is supported by JSPS Grant-in-Aid for Research Activity Start-up (no. 23840007). KSS is supported by the National Radio Astronomy Observatory, which is a facility of the National Science Foundation operated under cooperative agreement by Associated Universities, Inc.

REFERENCES

- Alaghband-Zadeh S. et al., 2012, MNRAS, 424, 2232
 Alberts S. et al., 2013, MNRAS, 431, 194
 Aretxaga I. et al., 2007, MNRAS, 379, 1571
 Barger A. J., Cowie L. L., Sanders D. B., Fulton E., Taniguchi Y., Sato Y., Kawara K., Okuda H., 1998, Nature, 394, 248
 Barger A. J., Wang W.-H., Cowie L. L., Owen F. N., Chen C.-C., Williams J. P., 2012, ApJ, 761, 89
 Bertin E., Arnouts S., 1996, A&AS, 117, 393
 Biggs A. D. et al., 2011, MNRAS, 413, 2314
 Blain A. W., Smail I., Ivison R. J., Kneib J.-P., Frayer D. T., 2002, Phys. Rev., 369, 111
 Blain A. W., Chapman S. C., Smail I., Ivison R., 2004, ApJ, 611, 725
 Bolzonella M., Miralles J.-M., Pelló R., 2000, A&A, 363, 476B
 Bruzual A. G., Charlot S., 1993, ApJ, 405, 538
 Calzetti D., Armus L., Bohlin R. C., Kinney A. L., Koornneef J., Storchi-Bergmann T., 2000, ApJ, 533, 682
 Capak P. L. et al., 2011, Nature, 470, 233
 Chapman S. C., Scott D., Windhorst R. A., Frayer D. T., Borys C., Lewis G. F., Ivison R. J., 2004, ApJ, 606, 85
 Chapman S. C., Blain A. W., Smail I., Ivison R. J., 2005, ApJ, 622, 772
 Chapman S. C., Blain A., Ibaraki R., Ivison R. J., Smail I., Morrison G., 2009, ApJ, 691, 560
 Chen C.-C., Cowie L. L., Barger A. J., Casey C. M., Lee N., Sanders D. B., Wang W.-H., Williams J. P., 2013, ApJ, 776, 131
 Condon J. J., 1992, ARA&A, 30, 575
 Coppin K. et al., 2006, MNRAS, 372, 1621
 Coppin K. E. K. et al., 2009, MNRAS, 395, 1905
 Daddi E. et al., 2009, ApJ, 694, 1517
 Downes A. J. B., Peacock J. A., Savage A., Carrie D. R., 1986, MNRAS, 218, 31
 Downes T. P., Welch D., Scott K. S., Austermann J., Wilson G. W., Yun M. S., 2012, MNRAS, 423, 529
 Dressler A., 1980, ApJ, 236, 351
 Eales S., Lilly S., Gear W., Dunne L., Bond J. R., Hammer F., Le Fèvre O., Crampton D., 1999, ApJ, 515, 518
 Ezawa H. et al., 2004, Proc. SPIE, 5489, 763
 Ezawa H. et al., 2008, Proc. SPIE, 7012, 701208
 Fazio G. G. et al., 2004, ApJS, 154, 10
 Greve T. R., Ivison R. J., Bertoldi F., Stevens J. A., Dunlop J. S., Lutz D., Carilli C. L., 2004, MNRAS, 354, 779
 Greve T. R. et al., 2005, MNRAS, 359, 1165
 Hainline L. J., Blain A. W., Smail I., Frayer D. T., Chapman S. C., Ivison R. J., Alexander D. M., 2009, ApJ, 699, 1610
 Hatsukade B. et al., 2011, MNRAS, 411, 102
 Hayashino T. et al., 2004, AJ, 128, 2073
 Hickox R. C. et al., 2012, MNRAS, 421, 284
 Hodge J. A. et al., 2013, ApJ, 768, 91
 Holland W. S. et al., 1999, MNRAS, 303, 659
 Hughes D. H. et al., 1998, Nature, 394, 241
 Ilbert O. et al., 2009, ApJ, 690, 1236
 Ivison R. J. et al., 2007, MNRAS, 380, 199
 Karim A. et al., 2013, MNRAS, 432, 2
 Kodama T., Tanaka I., Kajisawa M., Kurk J., Venemans B., De Breuck C., Vernet J., Lidman C., 2007, MNRAS, 377, 1717
 Kubo M. et al., 2013, ApJ, 778, 170
 Landy S. D., Szalay A. S., 1993, ApJ, 412, 64
 Lawrence A. et al., 2007, MNRAS, 379, 1599
 Lehmer B. D. et al., 2009, MNRAS, 400, 299
 Makovoz D., Marleau F. R., 2005, PASP, 117, 1113
 Matsuda Y. et al., 2005, ApJ, 634, L125
 Michałowski M. J. et al., 2012, MNRAS, 426, 1845
 Miyazaki S. et al., 2002, PASJ, 54, 833
 Postman M. et al., 2005, ApJ, 623, 721
 Rieke G. H. et al., 2004, ApJS, 154, 25
 Scott K. S. et al., 2008, MNRAS, 385, 2225
 Scott K. S. et al., 2012, MNRAS, 423, 575
 Shimizu I., Yoshida N., Okamoto T., 2012, MNRAS, 427, 2866
 Smail I., Ivison R. J., Blain A. W., 1997, ApJ, 490, L5
 Smolčić V. et al., 2012, A&A, 548, A4
 Sorba R., Sawicki M., 2010, ApJ, 721, 1056
 Springel V. et al., 2005, Nature, 435, 629
 Steidel C. C., Adelberger K. L., Dickinson M., Giavalisco M., Pettini M., Kellogg M., 1998, ApJ, 492, 428
 Steidel C. C. et al., 2000, ApJ, 532, 170
 Steidel C. C., Adelberger K. L., Shapley A. E., Pettini M., Dickinson M., Giavalisco M., 2000, ApJ, 532, 170
 Suwa T., Hirashita H., Tamura Y., 2010, Ap&SS, 330, 219
 Suzuki R. et al., 2008, PASJ, 60, 1347
 Tamura Y. et al., 2009, Nature, 459, 61
 Tamura Y. et al., 2010, ApJ, 724, 1270
 Tamura Y. et al., 2013, MNRAS, 430, 2768
 Uchimoto Y. K. et al., 2008, PASJ, 60, 683
 Uchimoto Y. K. et al., 2012, ApJ, 750, 116
 Wardlow J. L. et al., 2011, MNRAS, 415, 1479
 Williams C. C. et al., 2011, ApJ, 733, 92
 Wilson G. W. et al., 2008, MNRAS, 386, 807
 Yamada T., Nakamura Y., Matsuda Y., Hayashino T., Yamauchi R., Morimoto N., Kousai K., Umemura M., 2012, AJ, 143, 79
 Yun M. S. et al., 2008, MNRAS, 389, 333
 Yun M. S. et al., 2012, MNRAS, 420, 957

SUPPORTING INFORMATION

Additional Supporting Information may be found in the online version of this article:

Table 2. The AzTEC/ASTE SSA22 source catalogue.

Table 5. Information about identified counterparts.

Appendix A. Finding charts for the SMGs discovered by AzTEC/ASTE in the SSA22 field.

(<http://mnras.oxfordjournals.org/lookup/suppl/doi:10.1093/mnras/stu447/-/DC1>)

Please note: Oxford University Press are not responsible for the content or functionality of any supporting materials supplied by the authors. Any queries (other than missing material) should be directed to the corresponding author for the article.

This paper has been typeset from a $\text{\TeX}/\text{\LaTeX}$ file prepared by the author.